The Extended Distribution of Baryons around Galaxies

Joel N. Bregman[1] , Michael E. Anderson[2] , Matthew J. Miller[1] , Edmund Hodges-Kluck[1] , Xinyu Dai[3] , Jiang-Tao Li[1] ,
Yunyang Li[1,4] , and Zhijie Qu[1]
[1] Department of Astronomy, University of Michigan, Ann Arbor, MI 48109, USA; jbregman@umich.edu
[2] Max-Planck-Institut für Astrophysik, Karl-Schwarzschild-Str. 1, D-85748 Garching, Germany
[3] Homer L. Dodge Department of Physics and Astronomy, University of Oklahoma, Norman, OK 73019, USA
[4] Department of Astronomy, Peking University, Beijing 100871, People's Republic of China
Received 2017 August 2; revised 2018 March 21; accepted 2018 June 4; published 2018 July 17

Abstract

We summarize and reanalyze observations bearing on missing galactic baryons, where we propose a consistent picture for halo gas in $L \gtrsim L^*$ galaxies. The hot X-ray-emitting halos are detected to 50–70 kpc, where typically $M_{\rm hot}(<50\,{\rm kpc}) \sim 5 \times 10^9\,M_\odot$, and with density $n \propto r^{-3/2}$. When extrapolated to R_{200}, the gas mass is comparable to the stellar mass, but about half of the baryons are still missing from the hot phase. If extrapolated to $1.7R_{200}$–$3R_{200}$, the ratio of baryon to dark matter approaches the cosmic value. Significantly flatter density profiles are unlikely for $R < 50\,{\rm kpc}$, and they are disfavored but not ruled out for $R > 50\,{\rm kpc}$. For the Milky Way, the hot halo metallicity lies in the range 0.3–1 solar for $R < 50\,{\rm kpc}$. *Planck* measurements of the thermal Sunyaev–Zel'dovich (SZ) effect toward stacked luminous galaxies (primarily early type) indicate that most of their baryons are hot, are near the virial temperature, and extend beyond R_{200}. This stacked SZ signal is nearly an order of magnitude larger than that inferred from the X-ray observations of individual (mostly spiral) galaxies with $M_* > 10^{11.3}\,M_\odot$. This difference suggests that the hot halo properties are distinct for early- and late-type galaxies, possibly due to different evolutionary histories. For the cooler gas detected in UV absorption line studies, we argue that there are two absorption populations: extended halos, and disks extending to $\sim$50 kpc, containing most of this gas, and with masses a few times lower than the stellar masses. Such extended disks are also seen in 21 cm H I observations and in simulations.

Key words: galaxies: halos – Galaxy: halo – ultraviolet: galaxies – X-rays: galaxies

1. Introduction

During the past two decades, we have come to understand that galaxies are baryon-poor (e.g., McGaugh et al. 2010; Moster et al. 2010; Dai et al. 2012). That is, the dynamics of a galaxy (rotation curves or velocity dispersion) is interpreted within the framework of the Navarro–Frenk–White (NFW; Navarro et al. 1997) distribution to define its mass. This mass of baryons originally associated with this dark matter halo is given by the dark-matter-to-baryon ratio that is known to high accuracy from the cosmic microwave background (CMB) observation, about 5.3:1 (Planck Collaboration et al. 2014). The easily observed baryonic mass, the stars and cool gas, is significantly lower than the pre-collapse mass, by a factor of 2–100 (McGaugh et al. 2010). Evidently, the act of galaxy formation led to a fraction of the baryons falling deep into the potential well, becoming the familiar galaxies of today.

This situation has motivated a great deal of theoretical and observational work, with many of the observational efforts directed toward discovering the location and properties of the baryons that are "missing" from galaxies today (e.g., Guo et al. 2010; Davé et al. 2011; Piontek & Steinmetz 2011; Scannapieco et al. 2012; Vogelsberger et al. 2014; Schaller et al. 2015). One prediction for the missing baryons is that they reside in a hot state around galaxies (e.g., White & Rees 1978; White & Frenk 1991; Fukugita & Peebles 2006), with an extent as great as or greater than the dark matter halos. This gas acquires a temperature comparable to the dynamical temperature of the system by a combination of shock heating associated with infall plus heating from supernovae and active galactic nuclei (AGNs; e.g., Crain et al. 2015). The relative contributions of these heating agents are model dependent, but

each should leave different signatures, which involve the gas masses at different temperatures, the radial distributions of the gas components, and the metallicity distributions.

Observational efforts to study hot halos necessarily involve X-ray data, as the halos should be near their virial temperatures, $\gtrsim 10^6$ K for an $\gtrsim L^*$ galaxy, where nearly all of the important lines occur at X-ray energies. X-ray absorption line observations are confined to studies of the Milky Way halo, but emission-line investigations address both the Milky Way and external galaxies (O'Sullivan et al. 2007; Anderson & Bregman 2010, 2011; Anderson et al. 2013, 2016; Bogdán et al. 2013, 2015; Miller & Bregman 2013, 2015; Walker et al. 2015). Observations of gas well below the virial temperature are commonly seen in galaxy halos (e.g., Putman et al. 2012), at $\sim 10^4$ K for most of the UV absorption line gas, which is modeled as photoionized clouds (e.g., Werk et al. 2014). Some of the clouds of higher ionization state ions, notably O VI, may also be produced in collisional ionization from gas near $10^{5.5}$ K (e.g., Stocke et al. 2014). These gaseous components cannot be in hydrostatic equilibrium on the scale of R_{200}, so one expects the gas to fall to the disk on a relatively short timescale of about 1 Gyr. That would suggest that this gas is not a major mass component of the halo, but some results indicate otherwise (Werk et al. 2013).

One scientific goal of these observational programs is to obtain the density distribution of the hot gas, from which the gas mass can be determined. Another important goal is to measure the temperature of the hot halo, which reflects the effects of infall and feedback (e.g., Fielding et al. 2017; Qu & Bregman 2018). Feedback from stars is responsible for the metallicity in the halo, also of critical interest. Finally, the
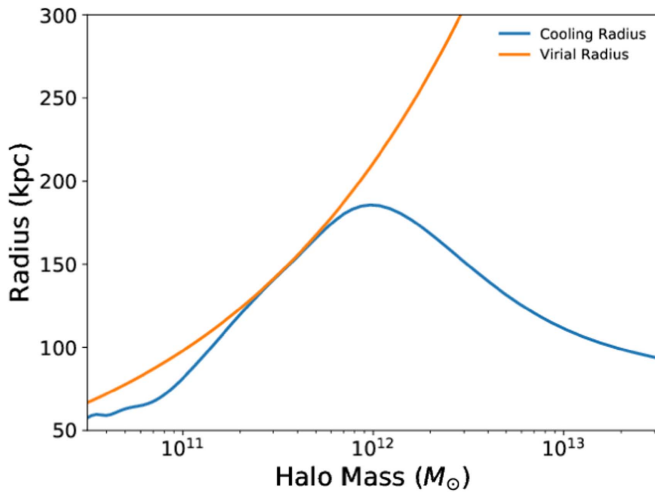
Figure 1. Virial and gaseous cooling radius as a function of gravitating halo mass for model `TCPIE` from Qu & Bregman (2018). The cooling radius lies in the 60–190 kpc range over a range of three orders of magnitude in gravitating halo mass.

Figure 2. Cooling and dynamical (freefall or sound-crossing) times as a function of radius for a Milky-Way-type galaxy where $\log M_{\rm halo} = 12.2$, $\log M_* = 10.8$, $R_{\rm vir} = 246$ kpc, and $T_{\rm gas} = 2 \times 10^6$ K (`TCPIE`, after Qu & Bregman 2018). The cooling time, which reaches a value of 10^9 yr at 30 kpc, is always longer than the dynamical time. The gaseous halo extends to $2R_{\rm vir}$ in the above model.

dynamics of the hot gas informs us of the infall or outflow, the turbulence, and the rotation of the hot halo, if present.

A variety of observational programs have made progress in these areas, and our goal is to synthesize these results into a coherent picture. In the first part of this paper, we consider the hot gas in the Milky Way and external galaxies (Section 2), with an analysis of the fraction of baryons within R_{200}. We also reconsider the importance of the cooler gas, seen in absorption in the UV (Section 3). Related observations bear on these issues, such as the Sunyaev–Zel'dovich (SZ) measurements from *Planck* (Section 4), which are sensitive to hot gas around the galaxies (Planck Collaboration et al. 2013) and to metallicity issues. We conclude by summarizing the current state of halo gas distributions, identifying areas of consistency and stress between investigations, arguing for a disk–halo model for extended gas distributions, and suggesting future observations (Section 5).

2. Hot Gas Density Distributions around Galaxies: Implications for Missing Baryons

For the analysis of hot gas, one usually assumes that the gas is near hydrostatic equilibrium at or above the virial temperature. When the temperature varies significantly less than the density, the gas density has a power-law dependence on radius beyond the core radius. This class of density profiles, the β-model (Cavaliere & Fusco-Femiano 1976), has functional form $n = n_o/(1 + (r/r_c)^2)^{3\beta/2}$.

To consider the validity (and other aspects) of such a model, we developed a semianalytic spherically symmetric model that has a hot gaseous halo near the virial temperature (Qu & Bregman 2018). The ionization state of the gas is modified by photoionization from the metagalactic radiation field (Haardt & Madau 2012), which changes the cooling function. A value of $\beta = 1/2$ is adopted, leading to $n \propto r^{-3/2}$ beyond the core radius. A cooling radius is defined in the usual way where the cooling time equals the Hubble time, and within this cooling radius the gas is assumed to cool at a rate equal to the star formation rate, which is given as a function of galaxy stellar mass by the star formation main sequence of star-forming galaxies (Morselli et al. 2016). For a metallicity of 0.5 solar, the
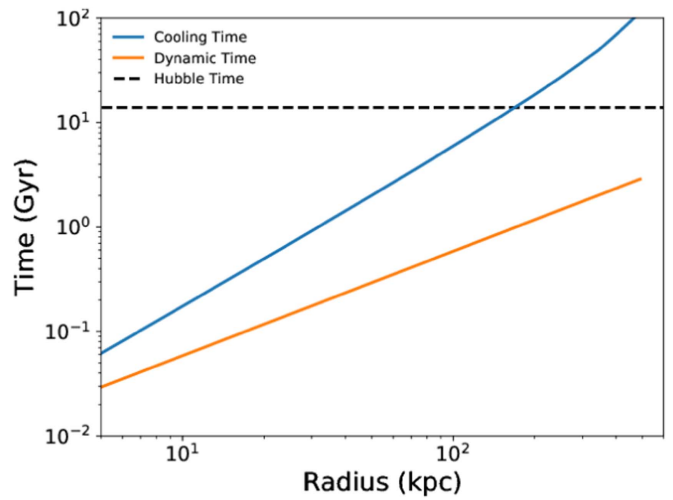
cooling radius occurs in the 60–190 kpc range (Figure 1) over a wide range of galaxy masses for cooling flow models with feedback where collisional ionization equilibrium is modified by photoionization (after model `TCPIE` of Qu & Bregman 2018). Also, the mass of the hot halo out to $2R_{200}$ increases approximately with the gravitating halo mass and is often comparable to and sometimes greater than the stellar mass. The radiative cooling time is longer than the freefall or sound-crossing time (similar values), supporting the use of the hydrostatic assumption (Figure 2). Also, a typical accretion velocity is $20\ {\rm km\ s^{-1}}$ (Miller et al. 2016), which is well below the sound speed of the gas, so ordered accretion does not have a significant effect on the density structure. We discuss suggested variations in the density law below.

There is a relationship between the temperature and β, and when the temperature varies less rapidly than the density and in the absence of turbulence, $\beta = T_{\rm rot}/T$, where $T_{\rm rot}$ is the thermal energy associated with the circular rotational velocity $v_{\rm rot}(r) = (GM(r)/r)^{1/2}$, which is similar to the virial temperature but varies with radius. A model with $\beta = 1/2$ implies $T = 2T_{\rm rot}$, although turbulent energy will also contribute, so we might expect that $T \leqslant 2T_{\rm rot}$, which is consistent with observations, as discussed below.

2.1. The Milky Way Halo Gas Density Distribution from X-Ray Absorption Line Data

At temperatures of $(1$–$2) \times 10^6$ K, the most important lines originate from the He-like and H-like oxygen ions (O VII and O VIII), with the O VII Heα resonant line at 21.60 Å being the strongest absorption line, followed by the O VIII Lyα resonant line at 18.97 Å, which has a fractional equivalent width (EW) that is about five times weaker for the same ionic column densities. The O VII ion is present over a broad temperature range, $5.4 < \log T < 6.5$ (from the peak ion fraction to an order of magnitude below the peak), while the O VIII ion is most common in the temperature range $6.1 < \log T < 6.8$. These and other lines have been detected in *XMM-Newton* and *Chandra* X-ray grating spectra against the continuum of bright

background AGNs (Nicastro et al. 2002; Rasmussen et al. 2003; Williams et al. 2005; Miller & Bregman 2013; Fang et al. 2015; Nevalainen et al. 2017). Here we concentrate on the O VII Heα line values, which have the most detections and highest signal-to-noise ratios (S/Ns) of any X-ray absorption lines.

There are few sight lines that pass through the bulge region, so constraints on the core radius have been poor when fitting a β model. One can either fix the core radius at a value typical for early-type galaxies (1–3 kpc) or use the form of the β model where $r \gg r_c$,

$$n(r) = \frac{n_0 r_c^{3\beta}}{r^{3\beta}}.$$

Miller & Bregman (2013) used the latter method, although both give the same results, within the uncertainties. For an optically thin plasma, $N(\mathrm{O\,VII}) = 3.48 \times 10^{14} \mathrm{EW\,cm}^{-2}$, where EW is in mÅ. The fitting leads to best-fit β values of $0.56^{+0.10}_{-0.12}$ if the lines are optically thin and $0.71^{+0.13}_{-0.14}$ if the lines are mildly saturated (Miller & Bregman 2013), assuming a Doppler width of 150 km s^{-1} for all observations. This resulted in saturation correction factors of $\approx$1–2, at about the 3σ level.

Using more recent data, Fang et al. (2015) assembled a larger sample of O VII absorption line measurements and found a correlation of the EW versus angle from the Galactic center for targets with $|b| < 45°$ at the 95% confidence level. However, they state that they do not find a strong correlation of EWs with Galactic coordinates. As this would seem to conflict with the findings of Miller & Bregman (2013), we examined whether it yields a significantly different result when fitting a β model to their data set.

The data set of Fang et al. (2015) consists of 33 O VII EW measurements from 43 sight lines. We exclude the 10 sight lines where no significant absorption was detected (reported as 3σ upper limits). The authors do not discuss whether these are primarily due to low continuum S/N or weak absorption features, although there are several indications that the former causes these nondetections. Many of these sight lines are projected near other sight lines with significant O VII detections. This implies that these sight lines should have detectable absorption if the absorption signature varies smoothly across the sky. Moreover, 8/10 of the nondetections occur in sight lines with counts per resolution element below the median sample value. Thus, the nondetections are likely due to low-S/N spectra, and excluding them should not bias our model fitting results.

Our hot gas density model and fitting procedure follow previous conventions discussed above. The hot gas electron density model is a modified β model defined as a power law extending to the virial radius as given above, where $n_0 r_c^{3\beta}$ is the normalization and 3β is the density slope.

We used a Markov chain Monte Carlo (MCMC) algorithm to explore the model parameter space and find a best-fit model. This code maximizes the likelihood between the model and data, where we define $\ln(L) = -0.5 \chi^2$. Thus, our best-fit model maximizes the likelihood and minimizes the χ^2. We bin the output chains from the MCMC code and treat these as probability density functions (pdf's) for each model parameter. The shapes and locations of the density function define the best-fit density model.

Our results are seen as pdf's and a contour plot in Figure 3. We define the best-fit model as the median value of each parameter pdf and give 1σ uncertainties as the 68% range away from the median value. The best-fit density model has

parameters of $n_0 r_c^{3\beta} = 1.20^{+2.13}_{-0.82} \times 10^{-2}$ cm^{-3} kpc$^{3\beta}$ (at solar metallicity and $\beta = 0.54^{+0.14}_{-0.13}$). Similar to Miller & Bregman (2013), these results include an additional uncertainty of 7.5 mÅ added in quadrature to the observed EWs to find an acceptable χ^2 (reduced $\chi^2 = 1.4$ with 30 dof). These results are also consistent with the aforementioned study by Miller & Bregman (2013), who found $n_0 r_c^{3\beta} = 1.30^{+1.60}_{-1.00} \times 10^{-2}$ cm^{-3} kpc$^{3\beta}$ (for solar metallicity) and $\beta = 0.56^{+0.10}_{-0.12}$.

More recently, Hodges-Kluck et al. (2016) compiled an updated set of O VII EWs for a study of Galactic rotation. They fit a disk plus halo gas model, where the disk component made a 10% contribution and led to a halo component with the parameters $n_0 r_c^{3\beta} = 1.43 \pm 0.25 \times 10^{-2}$ cm^{-3} kpc$^{3\beta}$ and $\beta = 0.53 \pm 0.03$, which is a significant improvement on the accuracy of the density normalization. To conclude, β-model fits to the samples of Miller & Bregman (2013), Fang et al. (2015), and Hodges-Kluck et al. (2016) are indistinguishable from each other and support a radially decreasing density profile with $\beta \approx 0.5$ for the optically thin case.

2.2. The Milky Way Halo Gas Density Distribution from X-Ray Emission Line Data

The absorption-line data set contains two to three dozen useful sight lines, but the emission-line data set for the Milky Way contains about 1800 sight lines (Henley & Shelton 2012, 2013), which lead to stronger constraints on the density profiles. For our analysis, we chose a subset of sight lines that avoid known bright objects (e.g., supernova remnants, clusters of galaxies) and avoid observations that might have problematic solar wind charge exchange contributions; this results in 648 sight lines for which both O VII and O VIII emission is available (Miller & Bregman 2015). Miller & Bregman (2015) considered the optically thin case and estimated a correction for optical depth effects.

In a recent work, we include radiative transfer effects for the O VII Heα triplet and the O VIII Lyα lines by using a Monte Carlo radiative transfer model (Li & Bregman 2017). Both a nonrotating halo and a rotating halo ($v_\phi = 183 \pm 41$ km s^{-1}; Hodges-Kluck et al. 2016) were considered, along with models that included disk components. The best-fit model includes rotation and a disk component, although the disk component is a minor mass component, as found previously; the O VII and O VIII fits yield the same results. This analysis was able to constrain the core radius, so that $r_c = 2.53 \pm 0.18$ kpc, which is consistent with the separate analysis of the inner part of the Galaxy and the Fermi Bubbles by Miller & Bregman (2016). The slope of the density distribution is 0.51 ± 0.02 with a normalization of $n_0 r_c^{3\beta} = 2.82 \pm 0.33 \times 10^{-2}$ cm^{-3} kpc$^{3\beta}$ (for a metallicity of 0.3 solar). Turbulence or motion is implied by the nonthermal component of the Doppler b parameter, where $b_{\mathrm{turb}} = 110 \pm 45$ km s^{-1}. For the disk component, the best-fit vertical exponential scale height is $z_h = 1.34 \pm 0.47$ kpc, and a radial scale length of 3 kpc was assumed. The exponential disk mass, $1.4 \times 10^8 M_\odot$, is small compared to the hot halo mass of $3.1 \times 10^{10} M_\odot$ within 250 kpc (Li & Bregman 2017).

The fits to the emission-line data do not put useful constraints on the metallicity, but constraints can be obtained when comparing the emission to the absorption-line data. That is because the emission depends on the integrated emission measure, Zn_e^2, while the absorption depends on the integrated column, Zn_e. In principle, this permits one to solve for the metallicity Z, but in practice a joint fit is difficult because the
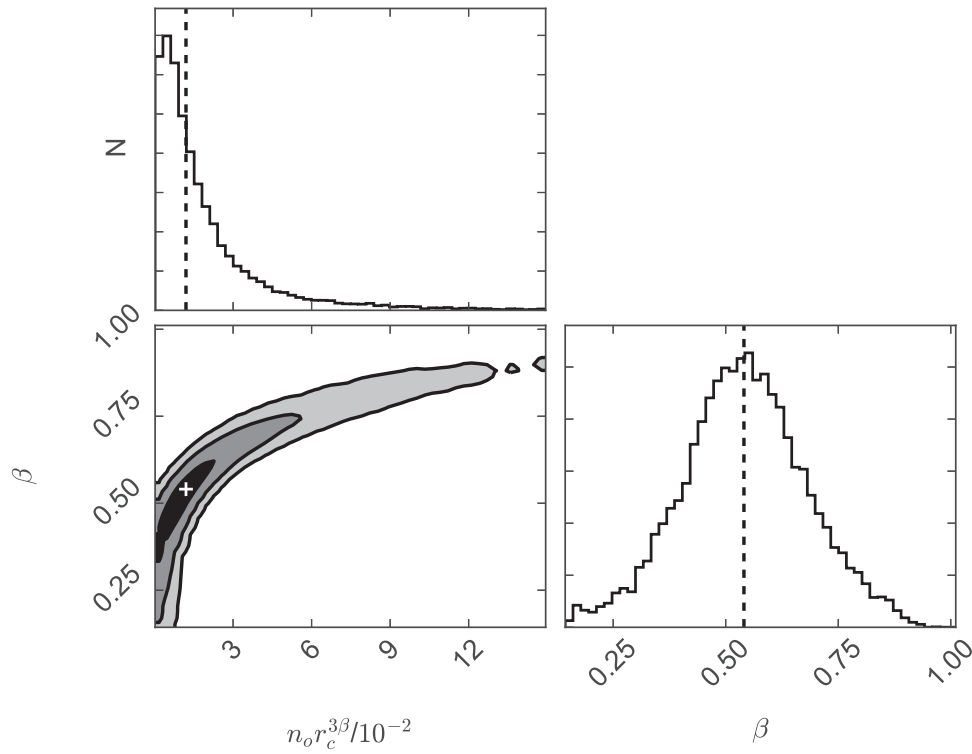
Figure 3. The pdf's and contour plot for our hot halo model parameters based on the data set of O VII absorption lines from Fang et al. (2015). The vertical dashed lines and white plus sign represent the median of each distribution, which we define as our best-fit model. The contour shades from black to gray represent the 1σ, 2σ, and 3σ regions. The results are the same as those determined by Miller & Bregman (2013) and Hodges-Kluck et al. (2016).

statistical power of the emission-line fits dominates a joint fit. Instead of a joint fit, we calculate model EWs from the emission-line models for different values of the metallicity; opacity effects are included. The EW sample is taken from Hodges-Kluck et al. (2016), which has 37 sight lines, from which we used only those sources where the S/N > 10 in the continuum near the O VII line. This removes low-S/N measurements with large errors, providing a sample of 26 lines of sight.

For each model, we calculate the χ_ν^2 value and a nonparametric measure of the fraction of EWs above or below the fit model (Figures 4 and 5). The probability of a certain fraction of observations randomly falling below/above a line is given by the binomial theorem. To obtain an acceptable χ_ν^2, we add to the EWs a line-of-sight variation along the lines of Miller & Bregman (2013), where we consider the values $\sigma = 5.0$ and 7.5 mÅ. At $Z < 0.3$, the χ_ν^2 value rises significantly above the best fit, and too many EWs lie above the model (Figure 4). The restrictions at high metallicity are weak, so we assume that the halo gas is unlikely to be supersolar, leading to a metallicity range of 0.3–1 solar, with a formal best-fit value in the middle of that range. This is in excellent agreement with the values deduced from Faerman et al. (2017) and Qu & Bregman (2018).

A separate analysis of the metallicity can be determined in the sight line to the LMC because we have both an electron column (from the pulsar dispersion measure) and an O VII EW (Wang et al. 2005; Yao et al. 2009; Fang et al. 2013; Miller & Bregman 2013, 2015; Hodges-Kluck et al. 2016; Miller et al. 2016). In the optically thin limit, this would lead to a metallicity for the hot gas phase of about 0.3 solar. When including optical depth effects, one must include the rotation of the hot halo, 183 ± 41 km s^{-1} (Hodges-Kluck et al. 2016), and
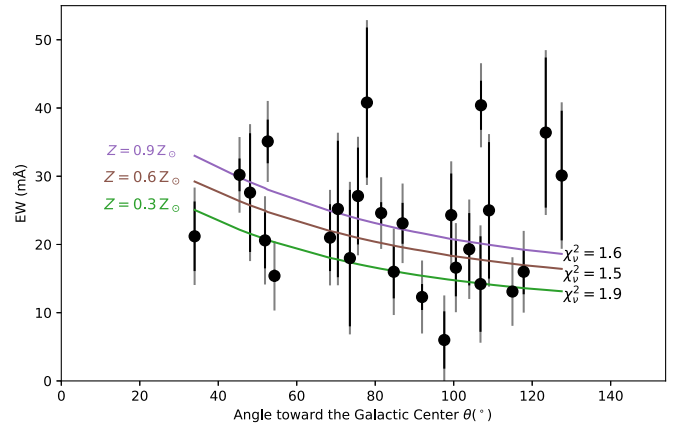

Figure 4. Distribution of O VII absorption line EW observations (Hodges-Kluck et al. 2016), with the addition of a 7.5 mÅ line-of-sight uncertainty, compared to the values inferred from the fits to the O VII and O VIII emission line measurements (Li & Bregman 2017) for different values of the metallicity (solid lines).

turbulent motion. The inferred metallicity of the gas is always greater than 0.6 solar, and for $b \approx 100$ km s^{-1}, the best-fit metallicity is solar (Miller et al. 2016). For a stationary halo, the metallicity would be about twice solar for the same Doppler b parameter.

2.3. The Density Models of Nicastro et al. (2016)

Nicastro et al. (2016) present an analysis of Milky Way O VII absorption line data, using both high-latitude sight lines (extragalactic) and absorption from low-latitude sources, which primarily lie in the disk and bulge. They present a variety of models, among which one (M3) contains the missing baryons
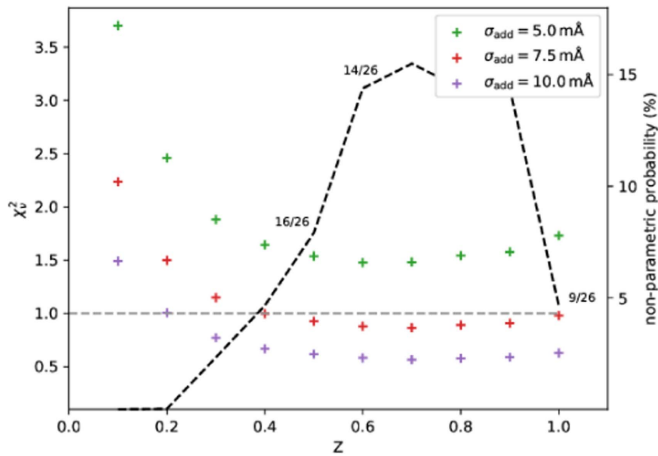
Figure 5. Quality of the agreement between the O VII absorption and emission line data, as a function of metallicity and for two different values of the additional line-of-sight variation in the EWs (σ_{add}). The plus signs represent χ^2_ν values (left scale) in fits to the emission lines, while the black dashed line shows the nonparametric probability (right scale), based on the number of points that lie above the model (numbers given at three points). For metallicities $Z < 0.3$, the χ^2_ν value rises significantly, and nearly all of the EW values lie above the model, indicating that $0.3 < Z < 1$.

in the Milky Way within a radius of $1.2R_{virial}$. We calculated the emission measure associated with model M3 at $b = 90°$ and find it to exceed the observed values by about an order of magnitude (this also occurs for other directions). Model M3 is a combination of an exponential cylindrical model (M2) and a spherical β model, where the first component produces an emission measure of $6.4 \times 10^{-2}\,pc\,cm^{-6}$ and the second component has an emission measure of $9.1 \times 10^{-2}\,pc\,cm^{-6}$, or a sum of $1.55 \times 10^{-1}\,pc\,cm^{-6}$ (toward $b = 90°$). This is 12 times greater than the high-latitude emission measure of $1.25 \times 10^{-2}\,pc\,cm^{-6}$ (McCammon et al. 2002) used as a point of comparison. This is also true for their model B, where the overproduction factor is 14.5 relative to the emission measure of $1.25 \times 10^{-2}\,pc\,cm^{-6}$. The overproduction factors are 37, 130, and 18 for models A (spherical β model), M1 (exponential spherical model), and M4 (spherical β model), respectively. We also compared the predicted O VII and O VIII line strengths, corrected for optical depth effects (Li & Bregman 2017), with the observed values (Henley & Shelton 2012, 2013) and found a similar discrepancy between their model and the data.

For their model M3, a combination of models A and M2, they used their best fit for model M2 and then fixed those parameters and added the spherical β model (A). They froze $\beta = 0.33$ and $R_c = 0$, although their best-fit values in the spherical β model were $\beta = 0.62$ and $R_c = 5.6$. This high-mass model does not consider the available parameter space, raising a uniqueness concern, so we searched for a self-consistent model. We used the emission-line data for the fitting, as they has many more sight lines and more statistical power than the absorption-line data. We corrected for optical depth effects as described in Li & Bregman (2017) and employed an MCMC fitting approach with a sample size of 1.2×10^6 and with the seven free model parameters (Figure 6). We fail to find a global best fit in that there are often multiple regions of comparable probability density. These regions of higher probability density usually do not correspond to the parameters adopted in model M3 of Nicastro et al. (2016). We cannot confirm the model of Nicastro et al. (2016), as it significantly

overpredicts the emission-line observations and because we cannot find a self-consistent solution to their favored high-mass model.

2.4. Constraints on the Density Distribution from Temperature Measurements

As discussed above, in hydrostatic equilibrium, $\beta = T_{rot}/T$, where T is the gas temperature and T_{rot} is from the rotational velocity. Therefore, measurements of T provide important constraints on the radial density distribution. One technique for determining the temperature of the Milky Way's hot gas component is to measure the O VIII-to-O VII absorption line ratio along background quasar sight lines. If one assumes that the O VII and O VIII lines originate from the same gas phase, the ratio of the column densities is a temperature diagnostic since the ion fractions of these species change relative to each other in the expected temperature range of the gas. Local O VIII absorption is detected less frequently than O VII absorption due to S/N limitations. However, there are well-known detections of local O VII and O VIII absorption in several quasar spectra, including 3C 273, Mrk 421, and PKS 2155 (Rasmussen et al. 2003; Williams et al. 2005; Nevalainen et al. 2017). From these O VII and O VIII EWs, column density ratios can be determined, from which we use standard collisional ionization models to infer temperatures of $(1.5–2) \times 10^6\,K$.

X-ray emission lines are also a useful diagnostic of the Milky Way's hot gas temperature and density distribution. Studies of X-ray emission lines, typically the same O VII and O VIII ions as absorption studies, have varied from single observations of a blank field of sky to comprehensive studies of the halo gas using X-ray observations covering the entire sky. For example, McCammon et al. (2002) observed a 1 sr region of the sky toward $l = 90°$, $b = +60°$ using a quantum calorimeter sounding rocket and were able to fit the spectrum of the absorbed soft X-ray background with a collisional ionization model with an emission measure of $3.7 \times 10^{-3}\,pc\,cm^{-6}$ and a temperature of $2.6 \times 10^6\,K$. Alternatively, Henley & Shelton (2013) measured the hot gas temperature by fitting 110 high-latitude *XMM-Newton* observations with collisional ionization plasma models (APEC). Their spectral fitting results include emission measures in the range of $(0.4–7) \times 10^{-3}\,pc\,cm^{-6}$ and a median temperature measurement of $2.2 \times 10^6\,K$, with an interquartile range of $0.63 \times 10^6\,K$. These temperature and emission measure constraints from X-ray emission studies are consistent with each other, but they differ slightly from absorption-line studies.

The minor discrepancy between the absorption and emission constraints on the halo gas temperature may not be significant, but it may indicate a temperature gradient to the halo gas. This is due to emission and absorption measurements weighting different parts of the halo since emission processes are proportional to n^2 while absorption processes are proportional to n (Figure 7). If we assume that the denser gas is closer to the center or plane of the Milky Way, the larger temperature inferred from the emission-line measurements is possibly representative of gas closer to the Milky Way as opposed to the lower temperature inferred from the absorption-line measurements. This is not a strong constraint, however, and thus we adopt a temperature of $2 \times 10^6\,K$ as being representative of the Milky Way hot halo at kiloparsec distances. This temperature is approximately the virial temperature for the Milky Way.
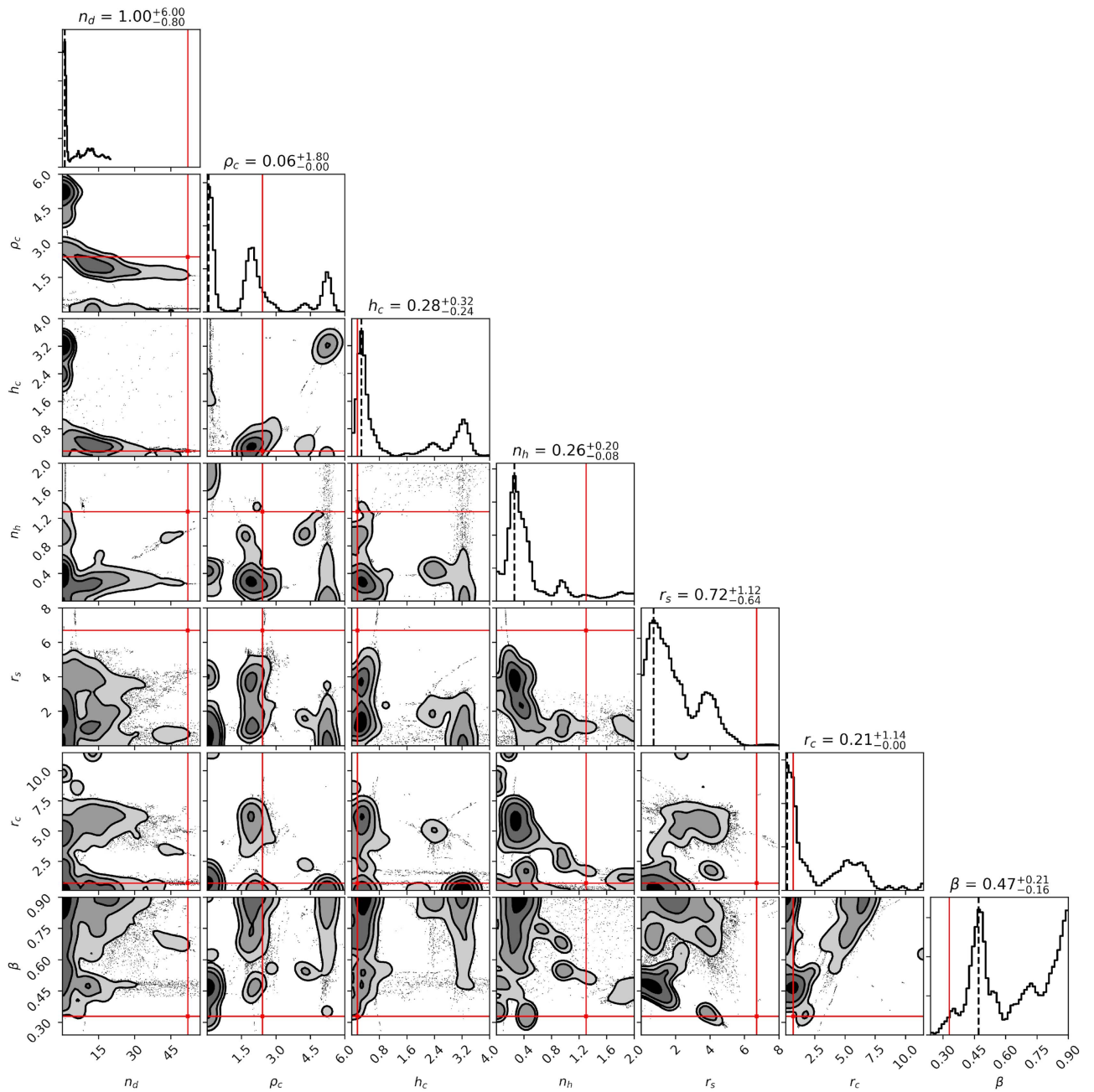
Figure 6. Probability density results of a fit of emission-line data to model M3 of Nicastro et al. (2016), which is their high gaseous halo mass model and is a combination of a spherical β model with a central cavity and an exponential cylindrical model. A best fit is not found, and the regions of high probability density usually do not correspond to the Nicastro et al. (2016) model values, shown as the intersection of two red lines.

One can determine the virial temperature from the rotational velocity of the Galaxy, taken to be $240\,\mathrm{km\,s^{-1}}$ (Bovy et al. 2014; Reid et al. 2014): $T_{\rm rot} = 1.4 \times 10^6\,\mathrm{K}$ at 20 kpc from the center. The precise radius used is unimportant because the rotational velocity changes slowly for an NFW profile. The ratio of $T_{\rm rot}$ to the observed halo temperature is approximately $T_{\rm rot}/T \approx 0.7 = \beta_{\rm spec}$, which is a bit steeper than the value inferred from the X-ray line studies. The difference may be attributable to turbulent motion providing additional support against gravity. The level of turbulent support that would bring $\beta_{\rm spec} \approx 0.5$ is a gas where the turbulent Mach number is about 0.5, which can occur in simulations (Fielding et al. 2017).

We consider whether it is possible to have density profiles that are significantly flatter than $\beta = 0.5$, as this has important

implications for the gaseous mass of the hot halo. In one of the flatter density distributions, Feldmann et al. (2013) have a temperature that rises to about $7 \times 10^6\,\mathrm{K}$ at 2 kpc from the midplane, decreasing to $4 \times 10^6\,\mathrm{K}$ at 10 kpc and $3 \times 10^6\,\mathrm{K}$ at 20 kpc (R. Feldmann 2018, private communication). Another flatter profile is given in the model of Kaufmann et al. (2008), where the halo is hot enough that the density has a radial dependence of about $n \propto r^{-1}$ for 15 kpc $< r <$ 50 kpc. For a hydrostatic model and a Milky Way potential, this would correspond to a temperature of about $4T_{\rm rot} \approx 6 \times 10^6\,\mathrm{K}$.

As the X-ray emission is dominated by material within 20 kpc of the disk (see below), due to the density squared dependence of the emission measure (Miller & Bregman 2015; Hodges-Kluck et al. 2016), these high temperatures would have
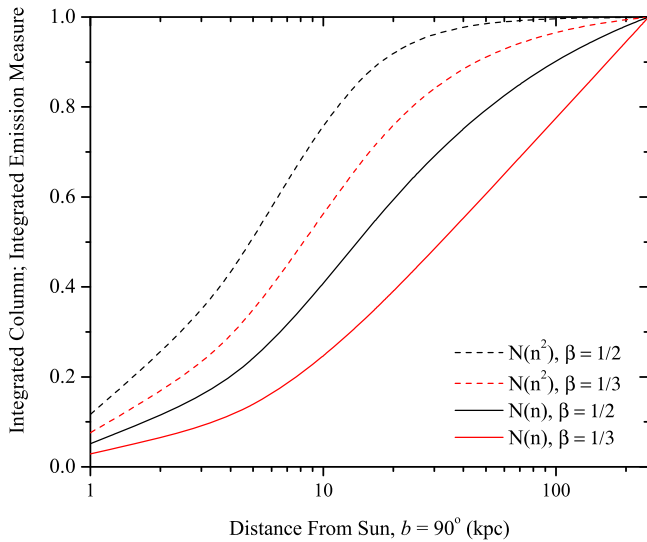
Figure 7. Column density and integrated emission measure, normalized to unity at 250 kpc, in the direction of $l = 90°$ for $\beta = 1/3$ and $1/2$. For $\beta = 1/2$, 50% of the emission lies within 4.9 kpc of the Sun and 90% within 17.6 kpc. For the column density, 50% lies within 14.0 kpc and 90% within 100 kpc. With $\beta = 1/3$, the 50% and 90% distances are 8.3 and 45.4 kpc for the emission measure and 32.2 and 168 kpc for the column density, respectively. This shows that Galactic O VII and O VIII absorption and emission studies are dominated by gas within about 50 kpc. Also, emission is more weighted by nearer gas than absorption.

a striking spectral energy signature (Figure 8). For the preferred halo temperature of about 2×10^6 K, the O VII emission is stronger than the O VIII emission. This relative line strength ratio would be reversed by 3×10^6 K, and at 5×10^6 K the O VII line is no longer detectable, while the Fe L complex becomes quite prominent. The general lack of the spectral energy signatures of higher-temperature gas (McCammon et al. 2002; Henley & Shelton 2013) argues against the models of Feldmann et al. (2013) and Kaufmann et al. (2008).

2.5. The Milky Way Gaseous Halo Mass Inferred from the Density Distributions

The mass of hot gas in the halo depends on the density distribution with radius, which is constrained in that we know the electron column density toward the LMC (Anderson & Bregman 2010). The density distribution is given by a normalization and, for a power-law distribution, a power-law index. Without further constraints, a degeneracy exists between the power-law density slope and the density normalization in the sense that the same electron column is obtained with a lower normalization and a flatter power-law distribution or a higher normalization and a steeper power-law distribution. The flatter density distributions lead to larger gas masses when the density law is extrapolated to the virial radius. As an example, for a density law of $n = n_0(r/r_0)^{-3\beta}$, the mass within 250 kpc is an order of magnitude higher for $\beta = 0.2$ than for $\beta = 0.6$ (Figure 9).

This degeneracy is the source of the controversy between authors for the gas mass contained within the virial radius of the Milky Way. When a fairly flat density law is considered ($\beta \approx 0.2$–0.3; Gupta et al. 2012, 2014; Faerman et al. 2017), the hot halo can contain the missing baryons, whereas for the models discussed by Miller & Bregman (2015) and Li & Bregman (2017), with $\beta \approx 0.5$, the gaseous halo mass is significantly less and does not account for the missing baryons
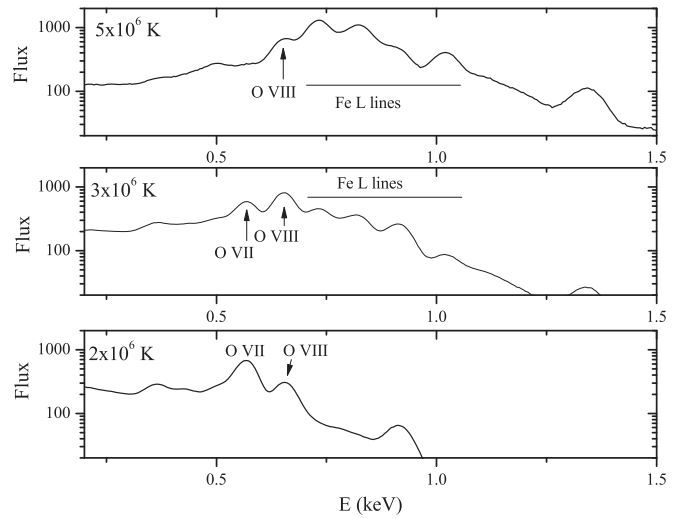

Figure 8. Model spectral energy distributions (count rates) at *XMM-Newton* resolution show dramatic changes as a function of temperature. Except for special directions (e.g., supernova remnant), observations resemble the bottom panel, a 2×10^6 K plasma, and exclude significant amounts of gas at higher temperatures within $\sim$30 kpc of the galaxy.
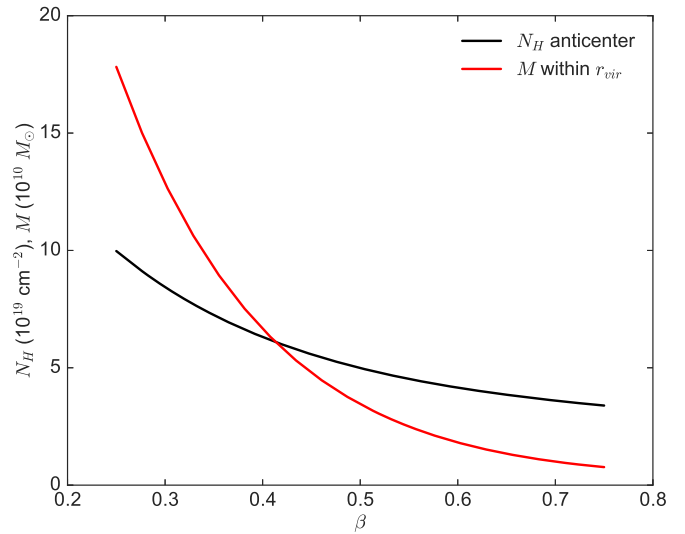

Figure 9. Hydrogen column density and gaseous mass from 10 kpc to the virial radius of 250 kpc. The models have a power-law density distribution, given by β, and all models are constrained to reproduce the pulsar dispersion measure to the LMC. For $\beta \approx 0.5$ (Miller & Bregman 2015), the hot halo accounts for only about one-third of the missing baryons. In very flat density distributions, $\beta \lesssim 0.25$, the hot halo could account for the missing baryons, which lie in the range of $(8$–$24) \times 10^{10}\,M_\odot$.

(about half are missing at R_{200}). This is seen in Figure 9, where the electron density is constrained to reproduce the pulsar dispersion measure, while we calculate the mass within 250 kpc and the electron column radially outward from the Sun to 250 kpc. At the lowest values of β (< 0.3), the gaseous halo mass rises into the range of the missing baryons, which has a value in the range of $(0.8$–$2.4) \times 10^{11}\,M_\odot$, depending on the assumed total mass for the Milky Way ($(1$–$2) \times 10^{12}\,M_\odot$; Xue et al. 2008; Gnedin et al. 2010; Watkins et al. 2010; Barber et al. 2014; Bland-Hawthorn & Gerhard 2016).

The challenge is to determine the power-law density index from other observations, and there are a few approaches to this problem. One method is to use information inferred from ram pressure stripping of dwarf galaxies or from the interaction of
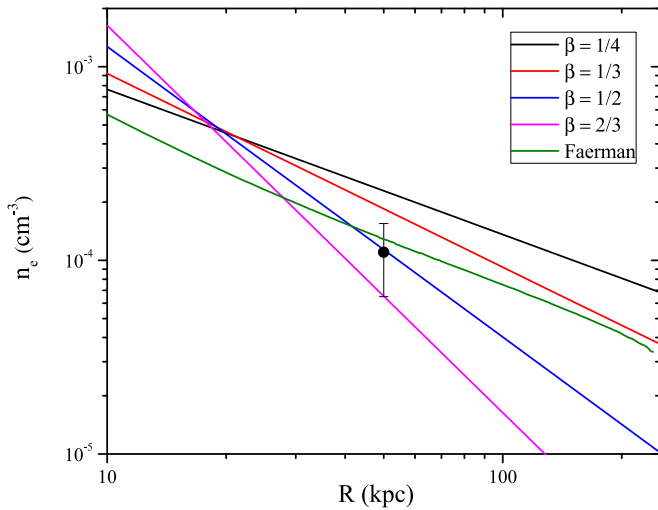
Figure 10. Power-law density distributions plus the density distribution from Faerman et al. (2017), normalized to reproduce the pulsar dispersion measure toward the LMC. The data point, from the numerical modeling of the LMC gas (Salem et al. 2015), is consistent with all but the flattest density distributions.

Figure 11. Ratio of the O VII column to R_{200}, from Miller & Bregman (2015) to the weighted average O VII column measured toward LMC X-3 and SMC X-1. As the two columns are nearly equal, a significant fraction of the column does not lie beyond the Magellanic Clouds. At the 3σ level, this implies that $\beta > 0.42$.

the Magellanic Clouds and the Magellanic Stream with the ambient hot halo. These require extensive hydrodynamic modeling and knowledge of the orbit of the object, along with the assumption that ram pressure is the primary physical process. The most thorough examination of this problem is by Emerick et al. (2016), who considered both ram pressure stripping and feedback effects from stimulated star formation. They find that these processes are unable to account for stripping (quenching) in less than 2 Gyr and discuss additional physics that might be included. This indicates that there is not a good understanding of gas loss from Local Group dwarf galaxies, so using them to infer the ambient density may be problematic, leading to significant uncertainties.

A different and promising approach to inferring the ambient density comes from a recent work that models the ram pressure on the leading edge of the LMC gas disk (Salem et al. 2015). By fitting their model to the detailed information available, they produce a particularly good density determination. Salem et al. (2015) give a gas density of $1.1^{+0.44}_{-0.45} \times 10^{-4}\,\mathrm{cm}^{-3}$ at $R \approx 50\,\mathrm{kpc}$.

Density constraints were also deduced in a model where there is a shock cascade between the Magellanic H I Stream and the ambient hot halo medium (Tepper-García et al. 2015). There are uncertainties in the inferred ambient density of a factor of two, plus the distance to the Stream may be larger than adopted, leading to further uncertainties in the hot ambient density. Therefore, we use the ambient halo density from Salem et al. (2015), which appears more secure. We compare the Salem et al. (2015) result to various density laws that are already constrained to reproduce the electron integral to the LMC (pulsar dispersion column) and find it to be consistent with all but the flattest of density profiles (Figure 10), requiring $\beta \gtrsim 0.3$.

To summarize, the observational data for the Milky Way point to $\beta \approx 0.5$, and after corrections for optical depth (Li & Bregman 2017), the hot gaseous mass of the hot halo is $M(<250\,\mathrm{kpc}) = (2.8 \pm 0.5) \times 10^{10}\,M_{\odot}$, similar to prior values (Miller & Bregman 2015), and the exponential hot disk mass is about 1% of the halo mass, with a value of $(1.8 \pm 0.3) \times 10^8\,M_{\odot}$. This hot halo gas mass is less than or
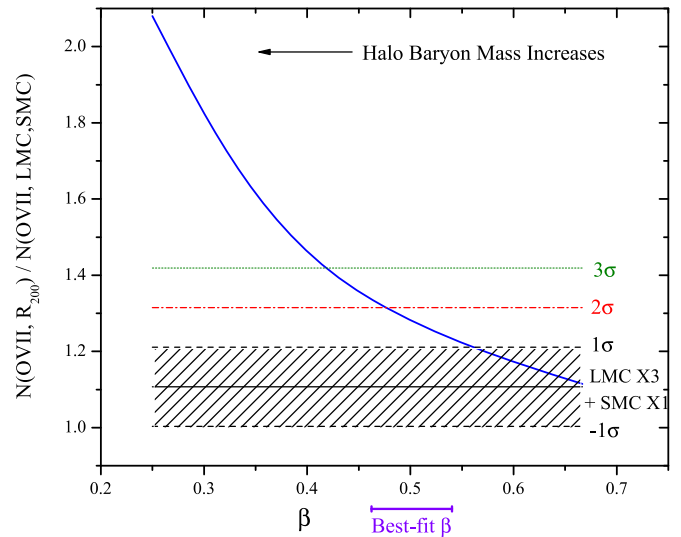
comparable to the stellar mass of the Galaxy and fails to account for the missing baryons by a factor of two (Miller & Bregman 2015; Salem et al. 2015; Li & Bregman 2017). A caveat here is that these tracers of the halo gas density are dominated by gas within 50 kpc, so if the gas density were to flatten beyond 50 kpc, a larger halo mass would occur. Such a flattening of the gas density at larger radii is suggested by Faerman et al. (2017), who show that with such a model the missing baryons lie within R_{200}. The hot gas component in their model is not characterized by a single value of β, but decreases from 0.35 (8 kpc) to 0.26 (70 kpc), slowly rising to 0.30 (180 kpc) and then rising up to 0.41 near the virial radius. The hot gas mass differences between models point out the necessity to constrain the shape of the density law in the range $0.2R_{200}$–R_{200} (50–250 kpc).

One of the few constraints for the density in this range comes from the realization that for the flatter density profiles ($\beta < 0.4$) there is a significant contribution to the column density in the 50–250 kpc range. We can obtain the column for $R < 50\,\mathrm{kpc}$ from the observation toward LMC X-3 and SMC X-1, for which we measure the observed O VII EWs from archival *XMM-Newton* data and obtain values of $23.1 \pm 3.0\,\mathrm{m\mathring{A}}$ and $21.0 \pm 4.9\,\mathrm{m\mathring{A}}$, respectively. The weighted mean of these two sight lines is $22.5 \pm 2.6\,\mathrm{m\mathring{A}}$. We can compare this to the EW inferred from background AGNs, which samples the entire halo out to and beyond R_{200}. Those observations toward AGNs, represented by the model of Miller & Bregman (2015), imply that the EW through the halo in that direction is $24.9\,\mathrm{m\mathring{A}}$. As this is nearly the same as the value toward the LMC/SMC objects, it limits the amount of the O VII column that lies beyond. To quantify this, we calculate the ratio of the column within 250 kpc to that within 50 kpc in the direction of the Magellanic Clouds, as shown in Figure 11. We find $\beta > 0.42$ at the 3σ level and $\beta > 0.34$ at the 5σ level, based on the weighted mean EW and the best-fit model EW to 250 kpc. This would rule out particularly flat density profiles, such as those of Gupta et al. (2012) or Faerman et al. (2017). However, there are two caveats. In addition to the statistical uncertainties used,

there can be significant line-of-sight variations in the absorption column (Miller & Bregman 2013), which we estimate to be 22% based on the variation of groupings of sight lines at similar Galactic latitude and longitude. This concern could be addressed by using several lines of sight toward the LMC and SMC, but such data are not available currently. Also, the above analysis assumes a constant oxygen abundance to 250 kpc, while a significant decline in the oxygen abundance beyond 50 kpc would lead to only a modest increase in the O VII EW even with a $\beta < 0.3$ profile.

To conclude, we do not find compelling evidence for a flattening of the halo gas density in the range 50–250 kpc, although further observations are needed to gain insight into this important issue. Without such a flattening, the gas within R_{200} fails to account for the missing baryons by a significant margin.

2.6. External Galaxies

The purpose of considering external galaxies is to determine whether their hot halo properties agree or disagree with the insights obtained from Milky Way studies. From X-ray studies, one obtains the surface brightness distribution, which can be converted to a density profile when a temperature and a metallicity are known. Temperature fitting requires more photons than obtaining a surface brightness distribution, while metallicity fitting requires about an order of magnitude more photons, with current X-ray instrumentation.

For the well-studied case of early-type galaxies, the temperature of the hot gas exceeds T_{rot}, typically by a factor of 1.4–2 (Davis & White 1996; Loewenstein & White 1999; David et al. 2006; Athey 2007; Pellegrini 2011; Goulding et al. 2016), presumably reflecting the additional heating of the gas from supernovae and AGNs (e.g., Gaspari et al. 2014). Observers also find that the temperature gradient is smaller than the density gradient, so for the isothermal case this leads to $d \ln(n)/d \ln(r) = -3T_{rot}/T$ (equivalent to $\beta = 0.5$–0.7 for the typical temperature ratio range; Goulding et al. (2016) give a median value of $\beta_{spec} = 0.6$).

This is similar to the density decrease that is inferred from the surface brightness decline, so there is consistency between the two methods. Where β derived from surface brightness measurements is smaller than T/T_{rot}, this may be an indicator that turbulent motion is an important component of the pressure support (e.g., Fielding et al. 2017).

Figure 12 shows the temperature, metallicity, and density profiles measured for three isolated ellipticals and three isolated spirals. This figure is adapted from Figure 14 of Anderson et al. (2016), with two new spiral galaxies added to improve the comparison. These are all galaxies more massive than the Milky Way ($M_* > 10^{11} M_\odot$) and have specifically been selected not to lie in larger galaxy cluster or group environments, so there is no contamination from an intracluster or intragroup medium.

In the temperature profiles, there is no clear difference between spiral and elliptical galaxies. At large radii ($r \gtrsim 20$ kpc), where the interstellar medium of the galaxy is no longer contributing to the observed signal, there is some suggestion that the spiral galaxies have cooler hot halos than the elliptical galaxies. Spiral galaxies inhabit lower-mass halos than elliptical galaxies at fixed stellar mass, so the observed result could reflect hydrostatic equilibrium with a lower-mass
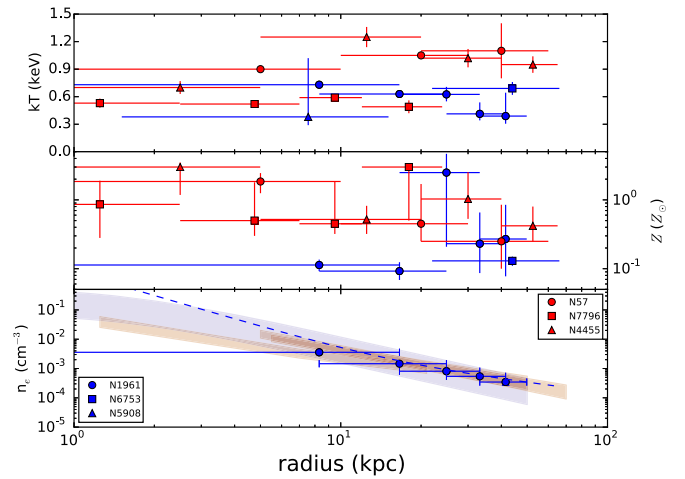

Figure 12. Temperature, metallicity, and electron distribution for three massive spirals (blue), two elliptical galaxies (NGC 57, NGC 7796, in red), and a massive early-type galaxy (NGC 4455, red); all are isolated systems. The temperature distribution is often isothermal, although there is a rise of T in NGC 4455 relative to the center and a decrease in T for NGC 1961. The metallicities of the early-type systems are generally larger than those of the late-type galaxies, with a median value of about 0.3 solar at 30 kpc. The density distribution is similar for all galaxies (red-pink bands are for early-type galaxies, and blue bands are for late-type galaxies; the dashed blue line is a $\beta = 0.5$ model).

halo for spiral galaxies (see also the discussion in Anderson et al. 2016).

The metallicity profiles show a clear difference between nonstarburst spiral and elliptical galaxies. The hot halos of the spiral galaxies NGC 1961 and NGC 6753 are clearly subsolar, at 0.1–0.2 $Z_\odot$, while the hot halos of the elliptical galaxies are close to solar abundance or even supersolar.

The radial density distributions of the hot halos around isolated nonstarburst spiral and elliptical galaxies are fairly similar. In general, the profiles are consistent with $n \propto r^{-3/2}$ (or $\beta = 0.5$), which is obtained over the distance range 10–100 kpc (Humphrey et al. 2006; Anderson & Bregman 2011; Dai et al. 2012; Anderson et al. 2013). This is also similar to the hot gas density distribution that is found in the optical regions of early-type galaxies (e.g., Athey 2007) but is a flatter distribution than found in clusters of galaxies (e.g., Vikhlinin et al. 2006).

For the individual massive spiral galaxies, NGC 1961 and UGC 12591, $\beta = 0.47 \pm 0.06$, $0.48^{+0.25}_{-0.08}$ and $T = (8.0 \pm 0.8) \times 10^6$ K, $(8.0 \pm 0.5) \times 10^6$ K, respectively (Anderson & Bregman 2011; Dai et al. 2012). Bogdán et al. (2013) examined the giant spiral, NGC 6753, and found a density profile corresponding to $\beta \approx 0.47$, similar to the other galaxies.

In addition to the three ellipticals shown in Figure 12, there are also observations of the isolated ellipticals NGC 720 and NGC 1521. For the extended emission around the isolated elliptical NGC 720, Humphrey et al. (2006) fit a profile that at large radii approximates to $\beta \approx 0.46$ and $T = (6.0 \pm 0.5) \times 10^6$ K (1–20 kpc). Humphrey et al. (2011) find a flatter profile, with $\beta \approx 0.41$. Anderson & Bregman (2014) show that the Humphrey et al. (2011) profile, which is based on a spectral analysis, overpredicts the observed soft X-ray surface brightness at all radii. The spatial analysis of Anderson & Bregman (2014) finds $\beta = 0.52 \pm 0.03$ and is consistent with the more modest hot halo found by Humphrey et al. (2006). For

Table 1
Summary of Hot Halo Properties

Galaxy	L_K ($10^{11}\,L_\odot$)	Hubble Type	$M_{gas}(<50\text{ kpc})$ ($10^9\,M_\odot$)	$M_{gas}(<R_{vir})$ ($10^{11}\,M_\odot$)	Z ($Z_\odot$)	References
NGC 1961	5.2	Sb/c	$5.0^{+0.2}_{-0.1}$	$2.3^{+0.3+5.1}_{-0.9}$	0.5	AB11
NGC 1961	5.2	Sb/c	11	11	0.12 (measured) B13	
NGC 6753	3.9	Sb	12	5.0	0.13 (measured)	B13
UGC 12591	5.6	S0/a	$4.4^{+0.7}_{-0.9}$	$1.5^{+1.6+3.0}_{-1.3}$	0.5	DAB12
Stacked luminous	$1.4^{+0.8}_{-0.4}$	⋯	$4.1^{+0.6}_{-1.0}$(stat) $\pm$ 2.9(sys)	⋯	0.3	AB13a
Stacked faint	$0.3^{+0.4}_{-0.1}$	⋯	$0.9^{+0.5}_{-0.4}$(stat) $\pm$ 0.6(sys)*	⋯	0.3	AB13a
Stacked early type	$0.7^{+1.2}_{-0.3}$	E and S0	1.9 $\pm$ 0.9 (stat) $\pm$ 1.3 (sys)	⋯	0.3 AB13a	
Stacked late type	$0.4^{+1.0}_{-0.2}$	Sabc & Irr	$1.2^{+0.5}_{-0.6}$(stat) $\pm$ 0.8(sys)*	⋯	0.3 AB13a	
NGC 720	1.6	E5	8 $\pm$ 1.5	1.6 $\pm$ 0.5	$\approx$0.6 (measured)	H06
NGC 720	1.6	E5	11 $\pm$ 2	2.7 $\pm$ 0.6	$\approx$0.6 (measured)	H11
NGC 720	1.6	E5	6.5 $\pm$ 0.5	0.8 $\pm$ 0.1	0.6 AB13b	
NGC 1521	2.3	E3	10	6	$\approx$0.4	H12

Note. Recent measurements of hot halo masses. For each column, L_K comes from the Two Micron All Sky Survey and the Hubble type from the NASA/IPAC Extragalactic Database. Best-fit measurements of the hot halo gas mass within 50 kpc and within the virial radius are then listed for each galaxy. In general, the mass within 50 kpc is fairly secure, while the mass within the virial radius depends on extrapolating the density profile out to much larger radii than it is observed. The errors quoted are statistical errors based on uncertainties in the surface brightness profile; other sources of error are discussed in the references for each paper (most of these other errors are folded into the systematic errors quoted for the stacked galaxies, however). Note that the asterisks on the stacked faint galaxies and the stacked late-type galaxies denote lower confidence that we are actually detecting and characterizing extended emission around these galaxies. For our measurements NGC 1961 and UGC 12591, the second listed uncertainty on the mass within the virial radius accounts for the possibility of a flattened profile, as discussed in the text. For the stacked galaxies, we do not extrapolate the mass to the virial radius since we do not have a strong measurement of the slope of the density profile. The second-to-last column lists the assumed (or measured, in some cases) metallicity used to convert the surface brightness profile into a gas mass (for NGC 720 and NGC 1251 a metallicity profile is measured, and we quote an approximate luminosity-weighted average). The references in the final column are: AB11—Anderson & Bregman (2011); B13—Bogdán et al. (2013); DAB12—Dai et al. (2012); AB13a—Anderson et al. (2013); AB13b—Anderson & Bregman (2014); H06—Humphrey et al. (2006); H11—(Humphrey et al. 2011); H12—Humphrey et al. (2012).

NGC 1521, the slope of their best-fit profile corresponds to $\beta \approx 0.44$ and $T = 6.0 \times 10^6\,\text{K}$.

These results were obtained from deep studies of individual objects, but we find similar results for stacked observations of large populations. The radial profile from stacking hundreds of nearby isolated early-type galaxies yields $\beta = 0.6 \pm 0.15$, and a similar stack of isolated late-type galaxies yields $\beta = 0.55 \pm 0.1$ ($L \geqslant L^*$; Anderson et al. 2013; see also Anderson et al. 2015).

Finally, we note that none of these studies extend to a significant fraction of the virial radius, so the total mass within the virial radius relies on an extrapolation. However, in every case there is no evidence for a flattening of the slope at large radius, which would be necessary in order for the extrapolations to significantly underpredict the total mass in the hot phase. Instead, Anderson et al. (2016) find that the X-ray surface brightness attributable to the hot gas shows a tentative steepening beyond about 20 kpc. In an analysis of NGC 720, there is also a tentative steeping at $r \gtrsim 25\,\text{kpc}$ (Anderson & Bregman 2014).

In Table 1 we summarize these observations of hot gaseous halos around isolated massive galaxies. In general, the trend is that more massive galaxies have more mass within 50 kpc and more mass inferred within the virial radius. It is unclear whether hot halos disappear below L^* or it just becomes too faint to be detectable. There also seems to be a hint of a trend such that elliptical galaxies have more hot gas mass than spiral galaxies, but there are not enough data points to make definitive conclusions.

A recent survey obtained *XMM-Newton* observations of five additional galaxies, which, together with UGC 12591, constitutes a complete sample of massive spiral galaxies in the local universe ($D < 100\,\text{Mpc}$; the CGM-MASS sample; Li et al. 2016, 2017, 2018); the median value is $M_* = 2.5 \times 10^{11}\,M_\odot$, and the median rotation velocity is about 330 km s^{-1}. This sample has a range in L_X of about 3, for galaxies with similar values of M_*, which is less than the factor of 30 range seen in lower-mass galaxies (O'Sullivan & Ponman 2004). The temperatures are in the 0.7–1.1 keV range, and the density distributions have a range of $\beta = 0.35$–0.68, with a median of $\beta = 0.45$. There is a relationship between the measured radial density distribution (β) and the ratio of the temperature inferred from rotation to the thermal temperature (β_{spec}), as physical arguments would predict. That is, systems that are hotter, relative to their rotational temperature, have flatter density distributions.

Using median values, $M_{200} = 8 \times 10^{12}\,M_\odot$, so $M_{baryon} = 1.3 \times 10^{12}\,M_\odot$. The median stellar mass is $2.5 \times 10^{11}\,M_\odot$, and the hot gaseous mass is slightly lower, at about $1.5 \times 10^{11}\,M_\odot$, so when including cooler disk gas, the measured baryon mass within R_{200} is $\approx 4 \times 10^{11}\,M_\odot$, or about 41% of the baryons. The remainder is unaccounted for and presumably lies beyond R_{200} or in a cooler phase, which we explore in the next section.

3. The Mass Contributions from UV-detected Absorbing Gas

Neutral and warm ionized gas is widely detected through UV absorption lines, where the interpretation of the absorption can infer a significant baryon mass (e.g., Werk et al. 2014; Prochaska et al. 2017). This gas is at $\sim 10^4\,\text{K}$ ($\ll T_{vir}$), so it is not buoyant, and if it is not supported by rotation, it would naturally sink into the galaxy at a rate of $M(H)/t_{ff}$, where $M(H)$ is the mass inferred in the halo and t_{ff} is the freefall time, about 10^9 yr. As the mass of warm halo gas has been suggested to be most of the missing baryons, about $10^{11}\,M_\odot$ for an L^* galaxy (Werk et al. 2014), the accretion rate would be $\sim 10^2\,M_\odot\,\text{yr}^{-1}$, which is far in excess of the observed accretion rates of such galaxies, generally less than $\sim 1\,M_\odot\,\text{yr}^{-1}$ (Leitner & Kravtsov 2011). For this reason, we consider whether having a large

warm baryonic mass in the halo is the only feasible interpretation.

There have been several works that examine the absorption properties of the region around galaxies. We consider the samples where a galaxy–AGN pairing is established before the spectroscopic observation, and where the galaxy is not selected based on gaseous properties. Also, we consider low-redshift systems ($z \lesssim 0.2$) and avoid samples devoted only to dwarf galaxy absorption, as they are significantly lower in mass than the X-ray-emitting galaxies, which are closer to L^*. Of the samples considered, both Bowen et al. (2002) and the targeted sample of Stocke et al. (2013) and Keeney et al. (2017) used relatively local galaxies ($z < 0.02$) and obtain H I column densities around galaxies with luminosities in the range of $10^{-2.5}$–$10^{0.2}$ L^*. The other sample considered is the COS-Halos program, which used Sloan Digital Sky Survey (SDSS) data to obtain galaxy–AGN pairings, for galaxies near and above L^*, and at a typical redshift of 0.2 (Werk et al. 2014; Prochaska et al. 2017).

3.1. H I Equivalent Width Distributions

We compare the samples of COS-Halos to that of the combination of Bowen et al. (2002) and the targeted absorption systems in Stocke et al. (2013) and Keeney et al. (2017) (henceforth the Stocke–Bowen sample) and find them different in important ways. The first comparison is of the EWs for the two samples, which are treated differently in the investigations. Multiple components in a single sight line are added together in the COS-Halos sample. There are usually multiple components for a sight line, as judged by low-ionization metal lines, but these components often blend together in the higher optical depth H I lines. Thus, separating such lines into components can be model dependent, especially at higher column densities. The Stocke–Bowen sample identifies individual components associated with a single galaxy, so we combine the individual components in order to make a comparison with the values from COS-Halos. Where the values were not listed, we extracted the EWs. Both samples are for systems with impact parameters less than 150 kpc.

The distribution of the EWs is significantly different between the local sample and the COS-Halos sample (Figure 13). Part of the difference is because the Stocke–Bowen sample has a number of galaxies with lower luminosities than the lowest-luminosity galaxy in the COS-Halos sample. This is significant because there is a correlation between galaxy luminosity and EW. When we just consider galaxies with $\log M_* > 9.4$, there is still a difference between the two samples as seen in Figure 14. In the Stocke–Bowen sample, there appear to be two systems with EWs above 1800 mÅ, while the rest are more than a factor of two lower (90–864 mÅ). Below we argue that these are separate populations and the lower EW sample has a median of 540 mÅ. The COS-Halos sample also has a set of large EW systems, so when we exclude the four with the largest values, the median EW is about 1100 mÅ, about a factor of two larger than the Stocke–Bowen sample. A factor of two difference in a saturated line corresponds to about a factor of 50 in the column density, since the EW is proportional to $\ln(N^{1/2})$. This assumes that the distribution of Doppler b parameters is the same in the two samples.

For the highest EWs, there is a dependence on radial distance and stellar mass in the Stocke sample. Both high-EW systems
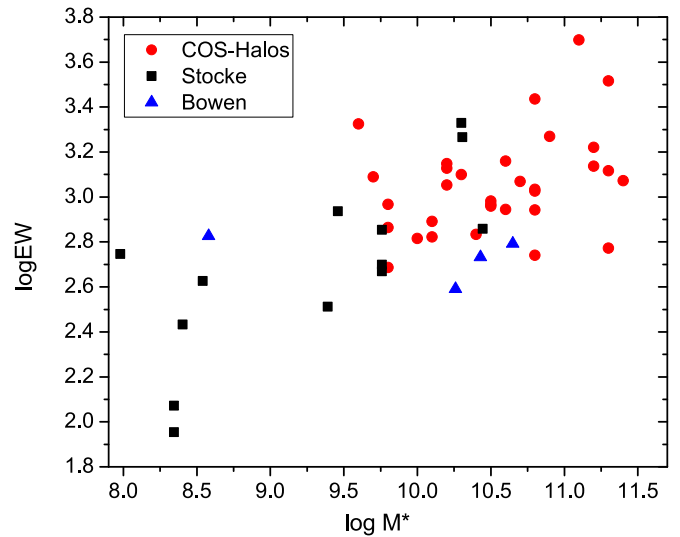

Figure 13. Distribution of H I Lyα EWs from Bowen et al. (2002), from COS-Halos (Werk et al. 2014; Prochaska et al. 2017), and from the targeted sample of Stocke et al. (2013) and Keeney et al. (2017). In the overlap region ($9.4 < \log M_* < 10.7$), the EWs of the COS-Halos absorption systems are generally larger than those of the Stocke–Bowen sample.
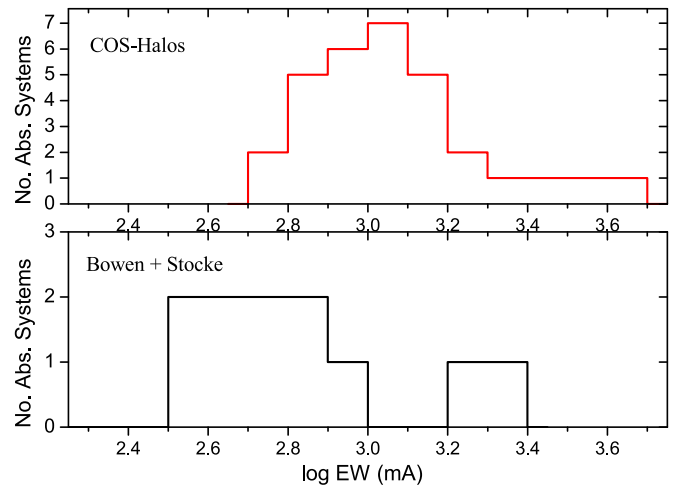

Figure 14. Distribution of EWs for the COS-Halos and the Bowen+Stocke samples for $R < 150$ kpc and $\log M_* > 9.4$. We interpret this as a high-EW extension plus a distribution of lower-EW systems, which could be consistent with separate disk and halo populations of clouds.

occur in their most optically luminous galaxies (Figure 13) and at relatively close radii ($r \leqslant 53$ kpc, whereas the sample median is 65 kpc). The Bowen sample does not have high-EW systems, but in the COS-Halos survey the highest EWs tend to occur among the more luminous galaxies (Figure 13).

3.2. The H I Column Density Distributions

The conversion of EWs to column densities can be uncertain owing to the presence of optical depth effects at moderate opacities that define the flat part of the curve of growth. This problem can be overcome if there are several lines of different opacity, permitting a curve of growth fit to be achieved. The situation is more challenging for a single saturated line, for which a lower limit can be assigned if there is no knowledge of the Doppler b parameter or of multiple components. However,
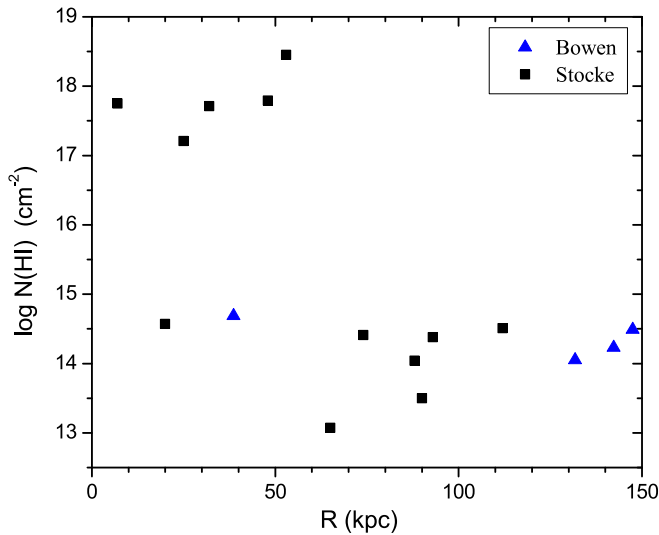
Figure 15. H I column density determined in the Stocke–Bowen sample as a function of impact parameter for the full range of M_* and for $R < 150$ kpc. The absorbers in the high column density population all occur for $R \leqslant 53$ kpc and may represent a disk component, while the lower column density, more extended absorbers may be a halo component.

Figure 16. H I column determined in the three samples as a function of stellar mass for $R < 150$ kpc. The lower column density sample of Stocke–Bowen is about 10^2 lower than the median of the COS-Halos sample where the samples overlap in stellar mass. The higher column density population may be similar between the two samples. The numbers next to the highest H I column density COS-Halos points show the impact parameter in kpc, where we note that most points lie within 50 kpc of the galaxy, except for three systems at 83–91 kpc. The highest column density point in the Stocke–Bowen sample has an impact parameter of 53 kpc.

if there are other low-ionization lines of lower opacity, the Doppler b parameter can be constrained, and that information is used in estimating a column density from an EW. Such information was brought to bear on the COS-Halos survey, in which they have obtained best estimates for N(H I). For the Stocke sample, Voigt profiles were fitted to the Lyα absorption lines, allowing for multiple components, procedures fully explained by Keeney et al. (2017). Bowen et al. (2002) also fit Voigt profiles and assessed the uncertainties through simulations.

The distribution of N(H I) can have large uncertainties in the Stocke–Bowen sample, but when examining N(H I) as a function of impact parameter (Figure 15), there is a bimodal distribution of the best-fit values, with a high column density grouping near 10^{18} cm^{-2} and a lower column near $10^{13.5}$–$10^{14.5}$ cm^{-2}. There is no dependence of this bimodal distribution on stellar mass (Figure 16). All of the high density systems have an impact parameter of 53 kpc or less, and five out of seven absorption-line systems within this impact parameter belong to the high column density family. In contrast, zero out of nine high column density systems lie beyond 53 kpc.

This bimodal distribution in column densities can be interpreted as a disk and a halo phenomenon. Warm and cool gas is found in disks in many galaxies, and the disk extends beyond the optical galaxy (e.g., Sancisi et al. 2008). Generally, the H I disk properties can be studied from 21 cm emission for column densities in excess of $10^{19.5}$ cm^{-2}, but there are a few studies that probe more deeply. Pisano (2014), using the Green Bank Telescope (GBT), studied NGC 2997 and NGC 6946, both of similar mass to the Milky Way and M31, to a limit of N(H I) $\sim 10^{18}$ cm^{-2}. For NGC 2997, the mean outer bound for H I detection is 50 kpc, while for NGC 6946, the outer H I boundary is about 45 kpc, but there is a filament to the NW that extends to about 80 kpc. Another L^* galaxy, NGC 2903, was observed with the Arecibo Observatory to a limiting H I column density of 2×10^{17} cm^{-2}, where the H I disk has a radial extent of about 60 kpc along the major axis and 40 kpc along the minor axis (Pisano 2014). Around more massive
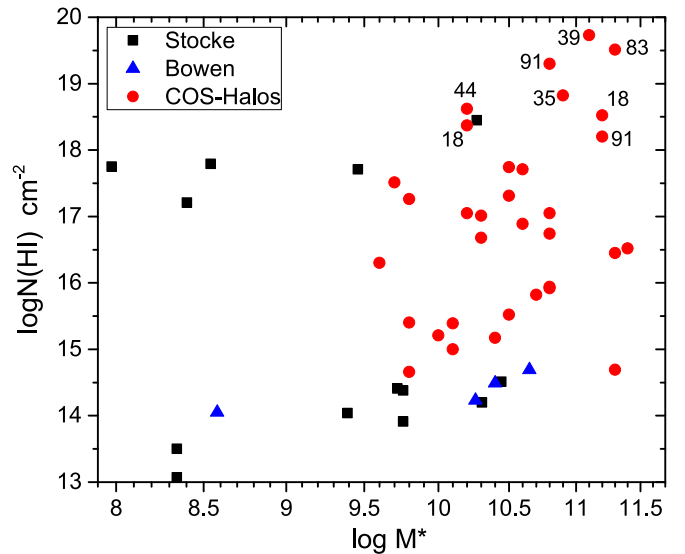
galaxies ($\log M_* > 10^{11} M_\odot$), an ongoing survey reports extended gas at distances of 50–100 kpc for about half of their nearby target galaxies, observed with the GBT (Ford & Bregman 2016). It appears that the H I disk commonly extends to about 50 kpc around L^* or more luminous galaxies for N(H I) detection sensitivities of $\sim 10^{18}$ cm^{-2} or lower.

The H I column densities found by Stocke et al. (2013) are below this value, and they are also larger in radius than typical higher column density 21 cm disks (Roberts & Haynes 1994; Sancisi et al. 2008). This suggests that lower-N(H I) gaseous disks can extend to about 50 kpc in this sample of galaxies, some of which are small and of low luminosity. The absorption systems with column densities less than 10^{16} cm^{-2} could be the counterparts of halo clouds seen in the Milky Way, which have a net mass significantly lower than the disk gaseous mass.

When examining N(H I) in the COS-Halos sample, the data may be consistent with there being two groups, one centered near $\log N$(H I) = 16.3 and a second group of seven objects in the range of $18.2 < \log N$(H I) < 19.8 (Figure 16). One can test whether a distribution is consistent with bimodality (Knapp 2007), and using the method of Pearson, the sample formally meets the criteria for being bimodal, although we do not find this to be compelling.

There are significant differences in N(H I) between the COS-Halos and Stocke–Bowen samples, much of which can be traced to the differences in EWs. The lower column density group from COS-Halos (N(H I) $< 10^{18}$ cm^{-2}) has a median significantly higher than the lower column density group in the Stocke–Bowen samples (N(H I) $< 10^{16}$ cm^{-2}) by about two orders of magnitude (Figure 16). This difference persists in the luminosity region where the two samples overlap. Most of this 10^2 difference is due to systematically higher EWs (a factor of $10^{1.7}$ in the column), with the remainder, a factor of two, due to either galaxy evolution or differences in the methods used to convert EWs to column densities. For the highest column
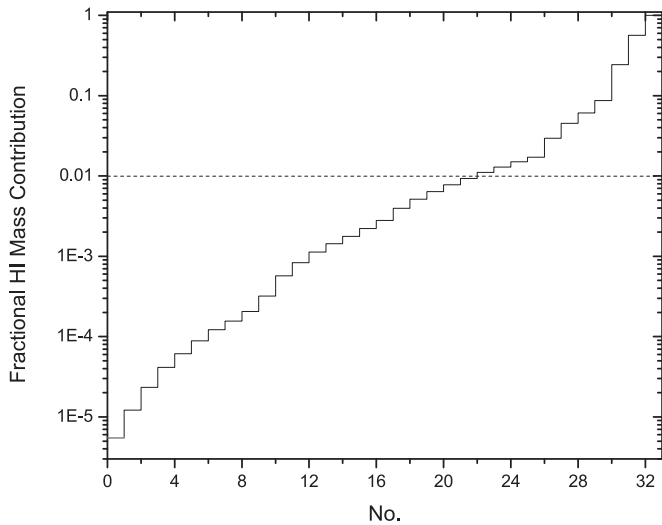
Figure 17. Cumulative sum of $N(\text{H\,I})R^2$ from the COS-Halos sample, normalized to unity. The systems with the two largest values of $N(\text{H\,I})R^2$ account for 75% of the total amount, and the top six systems account for 97% of the total amount.

density groups, the median value in the Stocke–Bowen sample is 17.9, while for the COS-Halos sample, it is 19.2, a difference of about a factor of 20. This difference is primarily due to the large EW values of galaxies with optical luminosities above those of the Stocke–Bowen sample (Figure 16).

Within the COS-Halos sample, the higher column density group is distinguished by the stellar mass of the galaxy. The eight highest H I column density systems have a median stellar mass of $1 \times 10^{11}\,M_{\odot}$, whereas the hosts for the lower column density systems have a stellar mass that is three times lower, $3 \times 10^{10}\,M_{\odot}$.

When considering the radial distribution of the high column density group in the COS-Halos sample, five out of eight lie within 50 kpc of the target galaxy (Figure 16), which can be understood as absorption by an extended gaseous disk. However, three absorption systems lie at about twice the distance of the inner group, 83–91 kpc from the target galaxy. We can obtain a rough estimate of the H I mass contributions from the various systems by calculating the product of $N(\text{H\,I})$ and the square of the impact parameter. In doing this, we see that just a few systems account for most of the H I mass. Two systems with impact parameters of about 83 and 91 kpc ($\log N$(H I) of 19.6 and 19.5) account for about 75% of the H I mass, and just six systems account for 97% of the H I mass (Figure 17). We inspect these systems individually to understand whether there is something special about their nature.

The two largest potential contributors to the net H I mass (the largest values of $N(\text{H\,I})R^2$) are the galaxy identifications 196_22 and 110_35, which we examine in more detail using archival images, including redshifts from SDSS (Figure 18). The system 196_22 ($z_{\text{gal}} = 0.2475$, $R = 83$ kpc; AGN J0925 +4004) has two small objects close to the AGN. This raises the concern that these closer, lower-luminosity objects could be the absorbing galaxies. Spectroscopic observations are needed to address this issue. The 110_35 system ($z_{\text{gal}} = 0.154$, $R = 91$ kpc; AGN J0928+6025 at $z = 0.29$) is part of a group of galaxies, of which two members are closer to the AGN (38 kpc and 48 kpc impact parameter). These two members are active star-forming systems, being relatively luminous in the UV *Galaxy Evolution Explorer* images, whereas the galaxy

assigned the absorption (110_35) is barely visible in the UV. It seems possible, if not likely, that the true absorbing systems are the spiral galaxies closer to the AGN. There are also a group of galaxies at the redshift of the AGN, which makes the image complex.

The third high column density system with a large separation is 177_27 ($z = 0.2119$, $R = 91$ kpc; AGN J0950+483), which does not have any moderately bright galaxies closer than 50 kpc. There is another galaxy to the east, which would have an impact parameter of 72 kpc if it were at the same redshift. Another system, galaxy 170_9 ($z = 0.3557$; sixth-largest value of $N(\text{H\,I})R^2$) is only 44 kpc away from the AGN J1009+713, suggesting a true association. However, a high-resolution image shows two galaxies at a separation of 15 and 20 kpc and with the same redshift as 170_9. It might not be possible to determine which is the true absorber without complementary H I maps, which are far beyond current capabilities.

This examination of the high-$N(\text{H\,I})$ systems at impact parameters >50 kpc suggests that two of the three systems (196_22 and 110_35) may have absorption attributable to nearer, less luminous galaxies. Excluding these two systems would decrease the net total H I mass by a factor of four. H I is occasionally seen distributed through galaxy groups at $z \approx 0$, such as in the Leo Group, so if this occurs at $z \approx 0.2$, it could explain the occasional high column density absorption far from a galaxy.

The H I masses can be inferred by adopting a characteristic column density and radius, where the mass is given by $M(\text{H\,I}) = 6.2 \times 10^7 (N(\text{H\,I})/10^{18})(R/50\,\text{kpc})^2\,M_{\odot}$. Of the high column density group of Stocke, a median system has a mass of $3.5 \times 10^7\,M_{\odot}$ out to 50 kpc. Only about 20% of the galaxies have high column densities, so when averaged over all galaxies, the value would decrease to $7 \times 10^6\,M_{\odot}$. For the lower column density absorbers in the Stocke–Bowen samples, the peak of the distribution occurs at $\log N(\text{H\,I}) = 14.3$, so $M(\text{H\,I}) = 1 \times 10^5\,M_{\odot}$ out to 150 kpc. In the COS-Halos survey, the high column density systems have a median near $\log N(\text{H\,I}) = 19.3$, leading to an H I mass of $1.2 \times 10^9\,M_{\odot}$ out to 50 kpc and $5 \times 10^9\,M_{\odot}$ out to 100 kpc. As these systems compose about 20% of the sample, the mean mass would be five times lower. The lower column density systems have a median $N(\text{H\,I})$ about two orders of magnitude larger than that in the Stocke–Bowen study, so the masses of this component are $1 \times 10^7\,M_{\odot}$ out to 150 kpc.

3.3. Total Hydrogen Column Densities

A calculation of the total absorbing mass requires a very significant ionization correction. This correction is nearly always obtained by adopting a photoionization model for the gas clouds. The properties of such absorbing clouds are poorly known, as they are not detected in emission, so sizes, densities, and filling factors are not independently known. However, the properties of the incident radiation field are estimated from the ensemble of AGNs and leakage from UV-bright galaxies (e.g., Haardt & Madau 2012), so a successful photoionization model fit yields the gas density and temperature, from which one can determine the gas pressure and the cloud size. The resulting cloud properties should be consistent with the ambient pressure expected in the halo (pressure equilibrium) and the observed sizes of clouds around the Milky Way, for example.

From the analysis for the COS-Halos sample (Werk et al. 2014), the pressure (expressed as nT) is surprisingly low for both
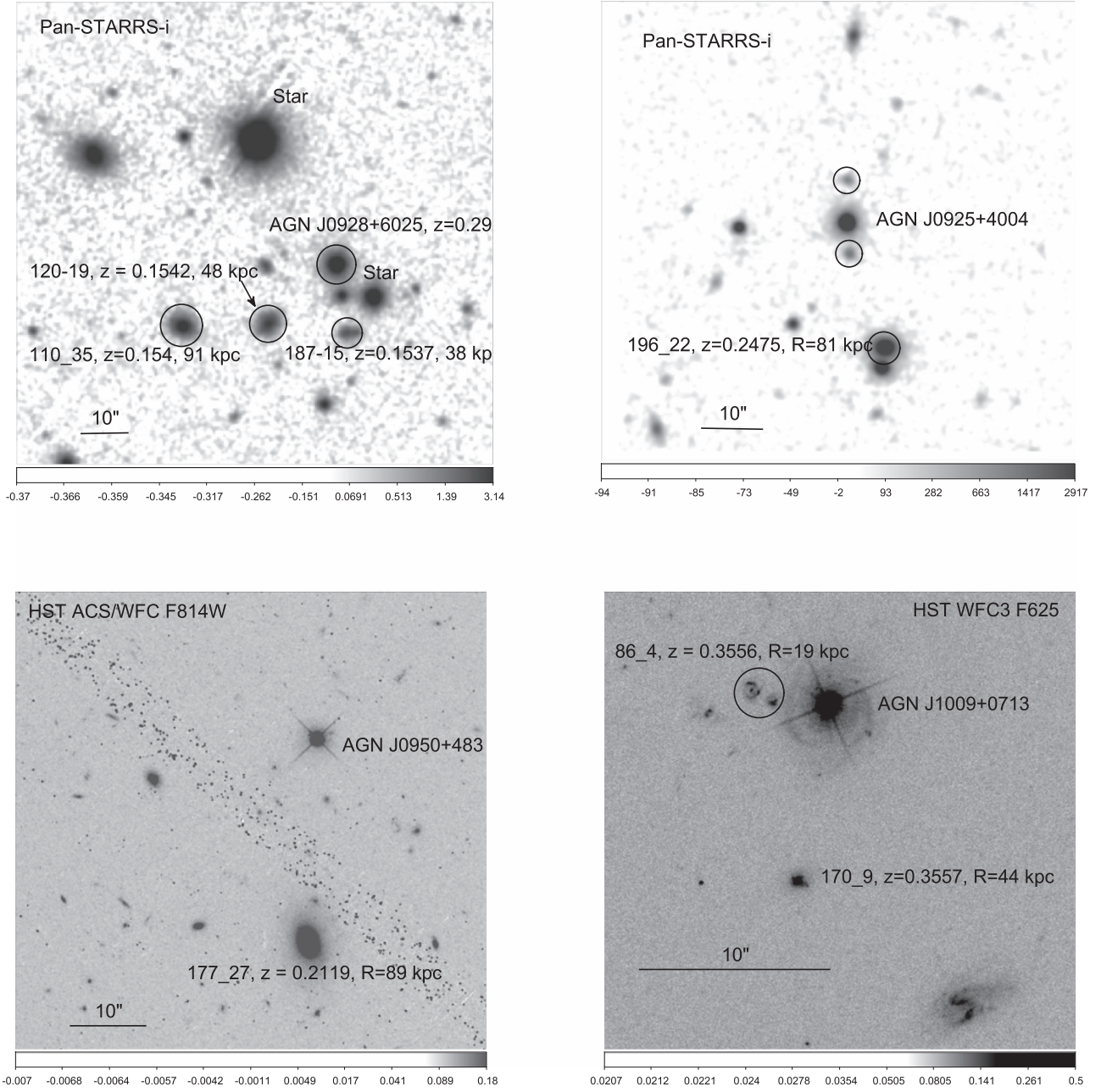
Figure 18. Optical images of four of the AGN–galaxy pairs that account for most of the H I mass, with the top two being the most important. The absorption attributed to 10_35 (top left) may be due to blue spirals closer to the AGN. Around the AGN J0925+4004 (top right), there are two nearby objects (circles, no redshifts) that are potential absorbers. Near AGN J0950+483 (bottom left) there are no obvious galaxies much closer than 177_27, except for the galaxy to the east with a separation of 72 kpc, if at the same redshift. Absorption against AGN J1009+0713 (bottom right) is assigned to galaxy 170_9, but it could be due to the two small galaxies projected 15–20 kpc from the AGN.

the high and low column density samples, with median values of 4 and $1\,\mathrm{K\,cm^{-3}}$, respectively. The characteristic pressure of a virialized system is $n_{200}T_{\mathrm{vir}} \approx 70(T/3 \times 10^{6}\,\mathrm{K})\,\mathrm{K\,cm^{-3}}$, much larger than the values determined from the photoionization model. The pressures inferred for the Milky Way hot halo are somewhat larger within 150 kpc (Salem et al. 2015; Faerman et al. 2017), generally more than two orders of magnitude larger than those from the photoionization analysis (for an incident photon flux of 3000 photons $\mathrm{cm^{2}\,s^{-1}}$). If one were to demand that the gas clouds have a pressure characteristic of their location in the halo, the flux of ionizing photons would be too small by the same large amount.

Another concern, also first identified by the COS-Halos team (Werk et al. 2014), is that the clouds and their masses can be enormous. Half of the clouds (16/33) have inferred lengths greater than 100 kpc, with two greater than 1 Mpc. About one-quarter have masses comparable to or larger than the stellar masses, in some cases by large amounts. Several in this group would have a baryon mass exceeding the cosmological value of the host system. These problems raise concerns with the photoionization analysis, which may reduce the reliability of the ionization correction that one would apply to the H I column to obtain the total hydrogen column.

Given these concerns, we adopt a median value for the conversion of $N(\text{H I})$ to $N(\text{H})$, based on the photoionization fits by Werk et al. (2014). This leads to $N(\text{H})/N(\text{H I}) \approx 400$ for the lower-$N(\text{H I})$ systems. The resulting values of $N(\text{H})$ are similar to what would be obtained by multiplying the metal column density for an ion (e.g., C, Si) by the metallicity correction, for a metallicity of about 0.2 solar. This conversion factor raises the gaseous mass for this ensemble of clouds to about $5 \times 10^9 M_\odot$ out to 150 kpc and a median column density per cloud of $6 \times 10^{18} \text{cm}^{-2}$. For the higher-$N(\text{H I})$ systems, the median conversion factor is about 6, so the hydrogen masses of these systems are $7 \times 10^9 M_\odot$ out to 50 kpc and $3 \times 10^{10} M_\odot$ out to 100 kpc (median column density of $1 \times 10^{20} \text{cm}^{-2}$). If averaged over the total number of galaxies, these masses are lowered by five, as only 20% of the galaxies have high column densities. However, these high-$N(\text{H I})$ systems occur in the highest-mass galaxies, and within that group, about half of the galaxies show such systems. Therefore, for a typical high-mass galaxy ($10.8 < \log M_* < 11.5$), these masses should only be lowered by about a factor of two.

For the targeted galaxy sample of Stocke et al. (2013), they calculate photoionization corrections for a subset and obtain $N(\text{H I})$-to-$N(\text{H})$ conversion factors that are very similar to those of Werk et al. (2014), with a median value of 450 and a lower conversion for two higher column density systems. For consistency, we use the same conversion factors as above and find that the low H I column density sample clouds have a mass of $5 \times 10^7 M_\odot$ out to 150 kpc, while the higher-$N(\text{H I})$ group has hydrogen masses of $2 \times 10^8 M_\odot$ out to 50 kpc.

To summarize, the absorption-line systems around targeted galaxies are consistent with being bimodal in $N(\text{H I})$ and can be understood as caused by two components: a halo of clouds that extends to at least 150 kpc, and an extended higher column density disk of gas that extends to 50 kpc, and in rare cases to 100 kpc. We propose metallicity and ionization conversion factors that, if correct, point to a picture where the mass of halo clouds is $\sim 5 \times 10^9 M_\odot$ (COS-Halos sample), while the extended disk has a mass of about $\sim 3 \times 10^9 M_\odot$ out to 50 kpc ($\sim 1 \times 10^{10} M_\odot$ out to 100 kpc). These extended halos are most frequently found in galaxies with $M_* \gtrsim 10^{10.8} M_\odot$. While these halo and disk gas masses are considerable, they are at least an order of magnitude less than the missing baryons, typically $\sim 10^{11} M_\odot$ for an L^* galaxy. Next, we will explore further implications of our assumed metallicity and ionization conversion factors and show that they satisfy other physical and observational constraints, such as producing the correct number of absorbing clouds and satisfying pressure equilibrium with the hot halo.

3.4. Number of Clouds in the Halo

The number of clouds and their sizes can be estimated through various approaches (e.g., Stocke et al. 2013), and here we offer another method. We suppose that the absorbing clouds are in pressure equilibrium with the hot ambient medium, which leads to a density of $n_{\text{cloud}} \sim n_{200} T_{\text{vir}}/T_{\text{cloud}}$. For a Milky-Way-type galaxy ($T_{\text{vir}} \approx 10^{6.3}$ K) and the usual temperature of a photoionized cloud (10^4 K), $n_{\text{cloud}} \sim 10^{-2} \text{cm}^{-3}$. We calculated a characteristic halo cloud hydrogen column density in the COS-Halos sample of $6 \times 10^{18} \text{cm}^{-2}$ (above), and for a spherical uniform cloud of radius r_c, the characteristic path length is $2^{1/2} r_c$, leading to $r_c \approx 5 \times 10^{20}$ cm (160 pc) and a cloud mass of $10^{3.6} M_\odot$. This implies that a typical L^* galaxy

halo contains $\sim 10^6$ clouds. If such a cloud were in the Milky Way halo, at a distance of 10 kpc (the high-velocity cloud [HVC]), the diameter would be $\sim 2°$, similar in size to some HVCs and the substructures seen in large HVC complexes. At these higher densities, photoionization would appear to be ineffective, but there is a successful alternative ionization model in which the ionization is driven by the turbulence and ultimately the motion of the clouds (Gray et al. 2015).

This calculation assumed that a single cloud produces the absorption, but multiple components are common around a single galaxy (Stocke et al. 2013; Werk et al. 2014). We can estimate the number of components along a galaxy sight line by using the covering factor or counting components, and we arrive at about the same result. For equal-size clouds and a covering factor of 90% (Werk et al. 2014), there would need to be an average of 2.4 clouds per line of sight in order for zero clouds to be observed 10% of the time (using Poisson statistics). Alternatively, one can try to count the number of components observed, although the ability to identify components depends on the ion, the S/N, and the optical depth of the feature. When we count individual components in the line profiles of Werk et al. (2013), we find an average of 2.2, and this would appear similar to that found by Stocke et al. (2013) in their targeted survey. For 2.3 clouds along the line of sight, and in pressure equilibrium as given above, the cloud radius is $\approx 4 \times 10^{20}$ cm (130 pc), and with a cloud mass of $\sim 10^{3.3} M_\odot$, similar to the values from the previous argument.

4. Constraints on the Baryon Content from the SZ Measurements

The thermal SZ effect is detected toward many rich galaxy clusters, yielding valuable information on the gas properties of these systems. As sensitivities improve, it opens the possibility that this method can provide information about the hot gas properties of galaxy groups and luminous galaxies, which we examine here.

The traditional Compton y parameter along a line of sight is $y = (\sigma_T/m_e c^2) \int P dl$, where σ_T is the Thomson cross section, m_e is the electron mass, c is the speed of light, and $\int P dl$ is the pressure integral along the line of sight. Clusters or galaxies are taken to be extended and treated as spherical objects at some distance D, so an integrated signal within a single beam is given by $Y_{500} = (\sigma_T/m_e c^2) k D^{-2} \int_0^{R_{500}} 4\pi r^2 n_e T dr$, where k is the Boltzmann constant and the subscript 500 denotes the value at the radius for which the overdensity of matter reaches 500 (e.g., Arnaud et al. 2010). For the typical convention where the virial radius is given by R_{200}, $R_{500} \approx 0.7 R_{200}$. For clusters of galaxies, where the density steepens and the temperature decreases significantly before the virial radius, Y_{500} is only 2% lower than the value that would be obtained if integrating to infinity, so this is a useful observational quantity. However, for galaxies, the temperature structure is not known near R_{500}, so it could be falling less rapidly. Also, where the density can be measured, it has a shallower radial decrease than in clusters, so the contribution to the Y parameter at larger radii is likely to be greater (Le Brun et al. 2015). In the case where the temperature is constant within the region of significance (to Y), the above parameter becomes $Y_{500} = (k \sigma_T/m_e^2 c^2) T M_e(R_{500}) D^{-2}$, where $M_e(R_{500})$ is the mass of electrons within R_{500}, but as we shall see, it will be necessary to consider larger radii for the case of
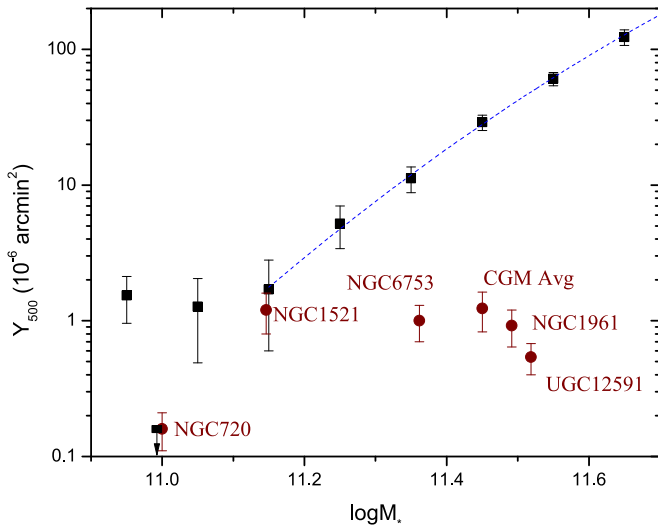
Figure 19. SZ Y parameter, normalized to a distance of 500 Mpc for the stacked galaxies (Planck Collaboration et al. 2013) and for the Y parameter inferred from the X-ray properties of five nearby massive galaxies (Table 1), plus a model galaxy that represents the average of the CGM-MASS sample (Li et al. 2017, 2018). For the two lower-mass galaxies, both of early type (NGC 720 and NGC 1521), the Y_{500} values are consistent with an extrapolation of the relationship from Planck Collaboration et al. (2013). At higher mass, the galaxies (all spirals) lie at least an order of magnitude below that relationship. For the spiral galaxies, the gas masses were calculated assuming 0.25 solar metallicity, and the error bars reflect a factor of two uncertainty in metallicity plus the uncertainties in extrapolating the gas mass to R_{200}.

galaxies. The value of Y_{500} is typically given in square arcminutes.

4.1. Planck SZ Detections of Stacked Galaxies

The most favorable galaxies for detection are massive ones, and since they are uncommon, Planck Collaboration et al. (2013) stacked many galaxies and found a signal using the 100–353 GHz bands, which has an angular resolution of about 10′. They bin their data by the mass of the stellar content, M_*, which they obtain from the catalog of Blanton et al. (2005), which is based on the SDSS galaxies. Approximately 260,000 galaxies are used in the SZ study, although above $\log M_* = 11.0$ there are 58,000 galaxies. They clearly detect the SZ effect for galaxies of mass $\log M_* \geqslant 11.25$, and it is likely that they detect the effect somewhat below that value.

An independent effort, using a similar approach, was taken by Greco et al. (2015). Their screening is a bit different, and they consider an additional correction, from the emission of dust grains within the galaxies, which makes only a modest difference. They smooth all frequency bands to 10′ resolution and then use aperture photometry, extracting a signal within $5R_{500}$. This procedure differs from that of Planck Collaboration et al. (2013), who left each map at the native resolution and fit functional forms of the pressure distribution. The resulting amplitude of Y_{500} is similar to that of Planck Collaboration et al. (2013), although their S/N is lower, so their signal is significant beginning at a slightly higher mass range.

4.2. Expected SZ Signal from X-Ray Observations of Massive Galaxies

There are few individual massive isolated galaxies for which there are good X-ray data of the hot gas, with the best cases listed in Table 1; supplementing this is the ongoing

CGM-MASS sample (Li et al. 2016, 2017, 2018). We can use these observations to calculate the SZ Y parameter for comparison with the stacked results from Planck (Planck Collaboration et al. 2013), which gives Y as a function of stellar mass (Figure 19). When calculating the SZ Y parameter for massive isolated galaxies with extended hot halos, we used the most recent gas mass and temperature determination (Table 1), although our result is insensitive to the choice of investigator results. The gas mass depends on the square root of the metallicity (approximately), but as the metallicity for the spiral galaxies has large errors, we use a value of 0.25 solar, which is within a factor of two of the range of measured values. For the early-type galaxies, NGC 720 and NGC 1521, we adopted the measured values, typically 0.4–0.6 solar (Table 1). Throughout an individual halo, we assumed a constant metallicity, temperature, and density power-law index. If the temperature decreases with radius, as is seen in galaxy clusters, our values of Y_{500} would be larger than their true values. A lower metallicity raises Y_{500}, with a factor of two decrease in metallicity raising Y_{500} by 40%. Neither of these uncertainties modifies the result (Figure 19) that the higher-mass galaxies have values of Y_{500} at least an order of magnitude below the stacked results (Planck Collaboration et al. 2013). The value of Y_{500} increases if the missing baryons are hot (either within or beyond R_{200}), with a typical increase in Y_{500} of a factor of three. This still is insufficient to account for the difference relative to the Planck results.

We consider the reasons for this discrepancy. One obtains the predicted value of Y from the observed relationships between the stellar luminosity and Y in large stacked data sets. For the stellar mass range of interest, about $10^{11.5} M_\odot$, both the stellar luminosity and Y are well measured, with uncertainties of less than 20%. The limit to the expected signal from individual galaxies is based on the maximum possible mass of gas, which in turn is inferred from the halo mass, the cosmological value of the baryon fraction, and the amount of baryons in stars and cold gas. The halo mass is inferred from the flat part of the rotation curve, coupled to an NFW profile for the dark matter distribution. For the halo mass to be incorrect by an order of magnitude, the rotation curve of NGC 1961 would exceed 800 km s^{-1}, which is never observed in the outer parts of galaxies. Another possibility is that the temperature rises beyond the radius at which the X-ray observations can no longer determine the temperature. However, if the temperature rose by even a factor of two, the gas would be unbound from the galaxy and flow outward, cooling by adiabatic expansion and decreasing the value of Y. It is likely that the gas temperature decreases with radius, in which case we have overestimated the maximum value of Y through our assumption of isothermality.

There have been some issues raised regarding the values of Y_{500} published by Planck Collaboration et al. (2013). They state that the Y_{500}–M_h relationship is self-similar, implying that the hot gas properties around a cluster of galaxies are similar to an individual galaxy. In particular, self-similarity implies the same shape for the density and temperature, as well as the same fractional baryon mass as a hot component. This is questioned by Greco et al. (2015) and Le Brun et al. (2015), who point out that the observed density profiles are flatter in individual galaxies than in galaxy clusters. Also, feedback will have a larger effect for galaxies than rich clusters. These arguments suggest that one might use a pressure profile for galaxies that is

flatter than for clusters when converting the Y signal within $5R_{500}$ to the value within R_{500}. While these are all sensible considerations, it leads to modest differences in Y_{500} for the galaxies of interest (Greco et al. 2015).

There may be other issues introduced by the observational requirement that the stellar mass is an independent variable. Wang et al. (2016) used new weak-lensing observations to estimate the effective halo masses of each stellar mass bin in the Planck Collaboration et al. (2013) sample and showed that there is both significant dispersion and significant model dependence in the distribution of halo masses as a function of stellar mass. With the weak-lensing data, they were able to account for some of this model dependence and renormalize the effective halo masses of each bin. This renormalization brought the $L-M$ and $Y-M$ relations in the stacking sample into agreement with the relations observed for galaxy clusters.

However, while Wang et al. (2016) showed that there is very little uncertainty in the behavior of mean properties in the stellar-to-halo mass relation (see also Behroozi et al. 2010; Moster et al. 2010), this is not guaranteed for the behavior of outliers. The fraction of elliptical and lenticular galaxies rises extremely sharply at stellar masses above $10^{11} M_\odot$ (e.g., Bernardi et al. 2010), and even among spiral galaxies, nearly all of them at the stellar mass of NGC 1961 are passive (Wilman & Erwin 2012), so a massive and moderately star-forming spiral galaxy like NGC 1961 is extremely unusual. Indeed, NGC 1961 is one of the most massive such galaxies known in the local universe.

Weak-lensing studies such as Velander et al. (2014) show that for spirals there is a nearly linear relationship between M_h and M_*, while for the red galaxies $M_h \propto M_*^{1.36}$, so the halo mass grows more rapidly with the stellar mass. For a stellar mass of $10^{11.5} M_\odot$ the red galaxies have a halo mass twice that of the blue galaxies. For a $Y-M$ relation with a slope of 1.61 (Wang et al. 2016), this translates to a factor of 3 in Y, which reduces the tension with the Planck data but does not wholly resolve the issue. Again, however, this observation relies on mean properties. If NGC 1961 is a factor of two below the mean halo mass relation for spiral galaxies, then the implied reduction in Y is a factor of 9.3 compared to the mean for ellipticals, which would largely resolve the discrepancy.

Fundamentally, the issue is probably how to compare results about isolated galaxies to results about central galaxies, even when the galaxies have the same stellar mass. Most of the X-ray results for hot halos are derived from studies of isolated galaxies, while the SZ results are measured for stacks of central galaxies. Numerical simulations can help to connect these two types of selection criteria, but it would be extremely informative to have observations that bridge this divide. This can include studies of larger samples of outliers, such as the CGM-MASS sample (Li et al. 2016, 2017), with moderate X-ray observations of six additional isolated giant spirals. Stacking of the SZ signal from samples of isolated galaxies, or deep SZ observations of individual systems, is also necessary to complement the X-ray results.

Another consideration is whether there is observational evidence for a significant amount of hot gas beyond the virial radius, due either to a group medium or to accretion filaments. The angular extent of the SZ signal suggests that galaxy groups or poor clusters may contribute. A luminous galaxy like NGC 1961 $(M_* = 3.1 \times 10^{11} M_\odot)$ has a virial radius of about 470 kpc, and at the mean distance of the sample, 500 Mpc,

this subtends a diameter of $6\farcm0$, which is less than the FWHM of the instrument, $10'$. Therefore, the galaxies should appear as point sources, but for the stacked images in the bins centered at $\log M_* = 11.15$, 11.25, the emission is somewhat extended (Planck Collaboration et al. 2013; Greco et al. 2015). The extent of the SZ signal is studied further by Van Waerbeke et al. (2014) and Ma et al. (2015), who use their weak galaxy lensing survey and perform a cross-correlation with the Planck data. Although their signal is at the 4σ level, they find that about one-third of the SZ signal comes from beyond the virial radius in their $M_h = 10^{12}-10^{14} M_\odot$ bin and one-half of the signal is beyond the virial radius for the higher-mass bin, $M_h = 10^{14}-10^{16} M_\odot$. This extended nature of the ionized gas is supported by kinetic SZ studies (Hernández-Monteagudo et al. 2015; Planck Collaboration et al. 2016), although the signal is weaker than the thermal SZ investigations, so the constraints are poorer.

To conclude, the SZ signal seen toward a set of stacked locally brightest galaxies suggests that a significant fraction of the galactic baryons are hot. However, for the observed stellar mass of NGC 1961 and other similar nearby massive spiral galaxies (and one early-type galaxy), the expected SZ signal is at least an order of magnitude below that inferred from the stacked ensemble. A resolution to this discrepancy may have a few components, such as the difference in the halo mass of early- and late-type galaxies of the same stellar mass, and an SZ contribution from hot gas beyond R_{200} but gravitationally associated with the galaxy (within the turnaround radius). However, it is possible that the selected high-mass spirals are not typical of the stacked galaxy sample from which the SZ signal is extracted. This suggestion can be examined further, such as extracting SZ signals from galaxy samples sorted by morphology or color.

5. Discussion and Summary

Several investigators have used different observations and conclude that they have found the "missing" baryons in individual galaxies, but some of these claims are mutually incompatible. The COS-Halos team uses their UV absorption line observations of warm ionized gas and argues that this component, within R_{200}, completes the baryon census for galaxies. For the phase with $T \sim T_{\rm virial}$, Faerman et al. (2017) offer a model for the Milky Way where the hot and warm baryons within R_{200} complete the baryon census. Gupta et al. (2012) have modeled X-ray absorption and emission line observations, with extrapolations, to account for all the Milky Way baryons within R_{200}. Nicastro et al. (2016) combine O VII absorption in the disk and halo, arriving at yet a different model for the hot gas distribution in the Milky Way, and with a hot gas mass that accounts for the missing baryons within about R_{200}. We argued that the hot gas mass within R_{200} does not account for the missing baryons in the Milky Way (Section 2.5). We find a similar result for external galaxies and conclude that to account for the missing baryons (Section 2.6), the hot halo would have to extend beyond R_{200}. Finally, SZ studies with Planck detect signals that extend beyond R_{200}, and the signal is easily strong enough to account for the missing baryons as hot gas, if the metallicity is low enough that X-ray luminosity limits are not violated (Section 4). Several of these results are in conflict with each other. Sorting out this situation was a primary motivation for this work.

Hot halos, as studied through X-ray-emitting and X-ray-absorbing lines, are fairly well understood for $R \lesssim 50$ kpc, where the temperature is about 50%–100% hotter than the virial temperature, $n \propto r^{-3/2}$ ($\beta = 1/2$), and the metallicity is about 0.1–0.5 solar, except for early-type galaxies where the metallicity is about solar. The mass within 50 kpc is $\sim 10^{9.5} M_{\odot}$, so determining the mass out to R_{200} (250 kpc) requires an extrapolation with a density model. Flattened density models ($\beta \lesssim 0.3$) lead to large gas masses, which, if correct, could contain the missing baryons within R_{200}. One such model was suggested by Nicastro et al. (2016), but we showed that this is in conflict with observed emission-line data, along with other issues (Section 2.3). The model of Faerman et al. (2017) cannot be ruled out, as the density law is consistent with most existing Milky Way observations (Section 2.5).

One can consider whether the density distribution of Faerman et al. (2017) is expected from models of galaxy assembly. Simulations of diffuse coronae in galaxies rarely show a flattening to the hot gas component with radius (e.g., Sokołowska et al. 2016), nor is it expected from general formation of structure considerations (Tozzi & Norman 2001). Structure formation models do not suggest the density distribution of Faerman et al. (2017).

Single galaxies do not produce a detectable SZ signal (Section 4), so stacks of galaxies were used, which produces a signal for massive galaxies ($\log M_* > 11.2$). These results indicate that much, if not all, of the missing baryons are hot and are extended beyond R_{200}. However, the observed signal is too large for the amount of baryons expected in the halos of giant spiral galaxies, inferred from X-ray observations. A possible resolution of this discrepancy is that there could be substantial differences in the hot gas halos around massive spirals compared to massive early-type galaxies. Until such issues are resolved, it will be difficult to use the SZ results to constrain the hot gas content of spiral galaxies.

5.1. UV Absorption Line Studies and a Disk–Halo Model

The UV absorption line studies are extensive, and we have added them to the analysis (Section 3), showing that there is a decrease in the EW and gas column density between $z \approx 0.2$ and $z \approx 0$ (between the COS-Halos and Stocke–Bowen samples). The larger H I EWs between COS-Halos and the Stocke–Bowen sample are also present with the COS-GASS survey (median $z = 0.039$; Borthakur et al. 2015, 2016), although to a lesser degree. For the region of overlap between COS-Halos and COS-GASS, impact parameters of 60–150 kpc, 9/10 of the highest H I EW systems occur in the COS-Halos sample. The median of the COS-GASS sample is about 25% below that of the COS-Halos sample, for the 60–150 kpc groups. The H I EW distribution of COS-GASS appears to be intermediate between COS-Halos and the Stocke–Bowen sample, where there is a factor of two difference in the median EW values.

One does expect a difference in EWs, due to evolution of gas in galaxies with cosmic time. The mass of dust at low redshift rises as a steep function of redshift for spiral galaxies in the *Herschel*-ATLAS survey, $M_{dust} \propto (1+z)^p$, where $p \approx 4$ (Bourne et al. 2012). Assuming that the dust mass is linearly proportional to the dust-bearing gas mass (mainly gas with $T < 10^{5.5}$ K), we see that a difference between $z = 0.2$ and $z = 0$ corresponds to a decrease in the gas mass of a factor of two. This leads to a decrease in the EW of about 25% for lines

on the flat part of the curve of growth. This decrease is consistent with the difference between the COS-Halos sample and the COS-GASS sample. However, the COS-GASS sample was selected for having a gaseous disk that was quantified with 21 cm observations, while the COS-Halos sample does not have this selection criterion. Therefore, adjusting the EWs between the two samples by the above method may not be valid because of the difference in sample selection criteria. In a comparison between the COS-Halos and Stocke–Bowen samples, the EW differences are significantly larger, the reason for which remains unclear.

We suggested that the absorption around galaxies can be interpreted as coming from two populations: a disk component, largely responsible for the high-N(H I) column densities within an impact radius of 50 kpc, and a more extended halo component. In the $z \approx 0.2$ study (COS-Halos), the mass of the disk component can be $(5-10) \times 10^9 M_{\odot}$, but they only occur in about 20% of the sight lines, whereas the halo clouds contribute about $5 \times 10^9 M_{\odot}$ in nearly all galaxies. This is significantly less than the estimate from the COS-Halos team but is similar to the value suggested in the analysis of Keeney et al. (2017).

A model that has striking similarities to the H I absorption line data around galaxies is from the *Illustris* simulation (Kauffmann et al. 2016). In a model closest to the Milky Way (their Figure 14), they show a column distribution with radius that appears to have two populations, one at about N(H I) $= 10^{19}$–10^{21} cm^{-2} out to about 50 kpc, and another in a broad range, N(H I) $= 10^{13}$–10^{17} cm^{-2}, that is steadily declining to R_{200}. Their model fails to reproduce the high column densities near 100 kpc that are found in COS-Halos, but we have suggested that most of those high column density detections at 80–92 kpc may not be associated with the target galaxies, which are much more massive than the Milky Way. If one excludes those few large-radius, high column density systems, the model and data appear consistent. The model could provide further insight if the absorption were identified with structures, such as a rotating disk of gas or halo clouds that may be falling in or flowing outward.

5.2. Comparison of Disk and Halo Gas of Local Galaxies with Absorption Samples

We compiled a comparison of the various extended gas mass determinations that appear in the literature, including the Milky Way (Zheng et al. 2015) and Andromeda (Lehner et al. 2015, 2017), along with our analysis of the Stocke–Bowen and COS-Halos samples (Table 2; note that the disk refers to the extended disk and does not include the H I in the optical disk). There are differences in the distances to which the gas is determined in each of these systems, so we needed to correct or extrapolate the masses to a similar distance for final comparison. To do so, we used the functional form of the density distribution for gas with $T < T_{virial}/4$ in the simulation of Fielding et al. (2017) for the galaxy with $M_{halo} = 10^{12} M_{\odot}$ and where we took the average of the low and the high feedback cases. From this simulation 90% of the halo gas lies within $0.33 R_{200}$ for the low-feedback case and $0.45 R_{200}$ for the high-feedback case. This would imply that if a significant fraction of gas lies beyond these radii, it is most likely beyond R_{200} and just projected onto the galaxy. The correction from $0.2 R_{200}$ to R_{200} is 2.3, while the correction from $0.5 R_{200}$ to R_{200} is just 5%.

Table 2
Halo Cool–Warm Gas Masses

Galaxy/Survey	R_{max} (kpc)	$M(\text{H I}, R_{max})$ ($M_\odot$)	$M_{gas}(R_{max})$ ($M_\odot$)	$M_{gas}(R_{200})$ ($M_\odot$)	Comments
Milky Way	15	6E7	2.8E8	1.5E9	$T < 1 \times 10^6$ K, Zheng et al. (2015)
Andromeda	50	4E7	1.2E9	2.8E9	Lehner et al. (2015)
Stocke–Bowen; halo	150	1E5	5E7		this work
S-B disk	53	7E6	5E7		this work
S-B total	150	7.1E6	1E8	1.1E8	this work
COS-Halos; halo	150	1E7	5E9		this work; 0.2 solar
COS-H; disk	50–100	1.2–5E9	7–30E9		this work
COS-H; total	150	1.2–5E9	1.1E10	1.2E10	this work
COS-H 2017	150		8.4E10	8.8E10	Prochaska et al. (2017)

This compilation shows that the Milky Way and Andromeda galaxies are similar and are similar to the COS-GASS results (Borthakur et al. 2015). The Stocke–Bowen masses are more than an order of magnitude smaller, while the COS-Halos masses are 5–40 times larger.

With most of the gas in the disk, the accretion rate is due to the mass of halo clouds, which have an infall time of ≈ 1 Gyr. That implies an accretion rate from the COS-Halos sample of about 5–$90\, M_\odot\, \text{yr}^{-1}$, whereas the observed median star formation rate for the COS-Halos sample is $1.3\, M_\odot\, \text{yr}^{-1}$. This would appear to lead to an increase in the mass of the disk with time. At the lowest accretion rate, the gaseous mass of a typical disk would double in 1–2 Gyr, while at the highest rate, the doubling time is <0.1 Gyr. However, the gaseous masses of disks have not increased significantly in the past 2.5 Gyr (see Putman 2017), the age difference between the COS-Halos sample and the local universe. One resolution to this issue is that a larger fraction of the "halo" clouds may be in a rotating disk and not accreting onto the galaxy. Unfortunately, these galaxies are too distant to be mapped in H I with current synthesis arrays.

5.3. Where Are the Missing Baryons?

The observations are generally consistent with a picture where the extended halo density declines as $r^{-3/2}$ and where the gas mass within 50 kpc is $\sim 5 \times 10^9\, M_\odot$. If extrapolated from 50 kpc to larger radii, it implies that the gas mass increases as $r^{3/2}$, or an increase by a factor of 11 from 50 kpc to 250 kpc, about R_{200} for the Milky Way. When increased by these amounts, the gas mass of $\sim 6 \times 10^{10}$ is comparable to the stellar mass, but the gas mass does not account for the missing baryons by a factor of 3–10, as discussed above. The Milky-Way-type galaxy might be surrounded by warm and neutral gas with a mass of $\sim 10^{10}\, M_\odot$, and when summed together with the other baryonic components, it is about half of the baryons. This raises the question of the location of the missing baryons.

One limiting case is to extrapolate the hot gas and the dark matter distributions until the ratio becomes the cosmological value. To do so, we use the NFW profile to extrapolate the dark matter out to and beyond the virial radius, which is a slowly increasing function of mass. For the gas, we assume that the density law does not change from the inner part, so $M_{gas} \propto r^{3/2}$. The reason that we consider this an extreme case is that we might expect the radial gas distribution to steepen and approach the dark matter density relationship at the radius where the cosmological baryon-to-dark-matter ratio is reached. Under these assumptions, we calculate the ratio of the increase in the M_{gas} to the dark matter mass, M_{DM} (Figure 20),
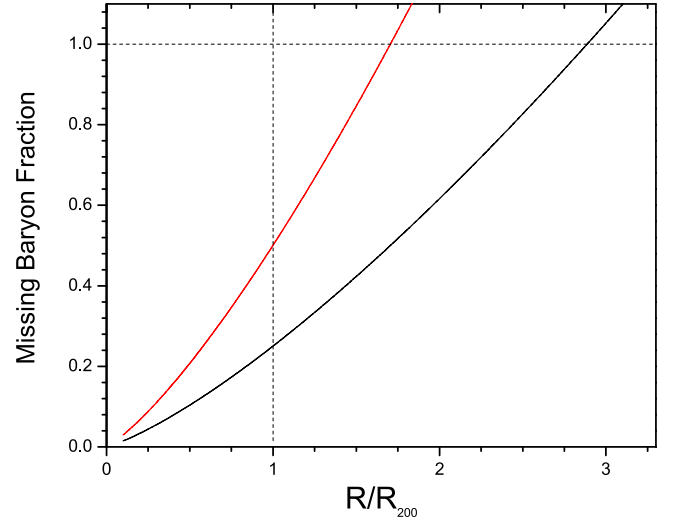

Figure 20. Fraction of the missing baryons relative to the dark matter content as a function of radius for the cases where the baryon fraction is 25% (black curve) and 50% (red curve) of the cosmic value at R_{200} (vertical dashed line). The horizontal dashed line is where all missing baryons are accounted for, which occurs at $1.7R_{200}$ and $2.9R_{200}$ for the two cases.

where we consider the two cases where 25% and 50% of the missing baryons are accounted for within R_{200}, which is fairly typical of our results. All of the missing baryons would be accounted for by about $1.7R_{200}$–$2.9R_{200}$. However, if the radial density law steepens with radius, the radius containing the missing baryons is moved further outward. Although $2R_{200}$ is the classical turnaround radius, dark matter simulations in a ΛCDM universe find the zero velocity surface to typically lie at $4R_{200}$–$5R_{200}$ for an isolated system (Busha et al. 2005). This is also the typical size of a galaxy group. A hot group medium would have a broader radial distribution than for individual galaxies, and that signature may have been detected in O VI and broad Lyα absorption by Stocke et al. (2014), although the galaxy group interpretation remains inconclusive (Stocke et al. 2017). To determine the fraction of baryons that are bound or unbound to a galaxy will require a detailed census of the gas mass as a function of temperature. For gas above about 5×10^5 K, this will require absorption studies of the X-ray lines (O VII, O VIII) at a level currently beyond the capabilities of current observatories (Bregman et al. 2015).

5.4. Future Observations

There are a number of observational issues to be resolved, such as those regarding SZ studies and UV absorption line

work. For the SZ work, one would like to consider the signal as a function of galaxy type or color, provided that there are sufficient numbers of objects for such an analysis. Greater angular resolution in SZ studies, such as from ongoing ground-based work (ACT, Swetz et al. 2011; SPT, Carlstrom et al. 2011), could help to determine the size of the hot gas region. The Stage 4 CMB program, CMB-S4 (Abitbol et al. 2017), will offer enormous advantages but will still require the stacking of galaxies to obtain a detectable signal. Today, it may be possible to examine nearby galaxies, such as M31 for an SZ signal (Taylor et al. 2003), provided that one can make sufficiently accurate Galactic foreground corrections.

From the wealth of UV absorption line data, there are issues relating to absorption from lower-luminosity galaxies near the line of sight, as discussed by Bowen et al. (2002). This is challenging but necessary work, which does not always lead to a unique result.

Further observational progress is possible, with the greatest improvements from new instrumentation in the X-ray band. One goal is to conduct an analog to the UV halo absorption line studies in X-rays for lines that cover a range of temperatures, such as the resonance lines of O VII, O VIII, C V, C VI, and N VII. This will become possible with an order-of-magnitude improvement in line detection sensitivity, which will be possible with the proposed Explorer concept *Arcus* (Smith et al. 2016), the approved ESA L-class mission *Athena* (Barcons 2015), or the NASA large strategic mission concept *Lynx* (Gaskin et al. 2016). Another goal would be to image the hot coronal gas in X-ray to a significant fraction of R_{200}. This is technically challenging because of the various X-ray backgrounds and long observing times, but *Athena* and *Lynx* should give us important new insights.

ORCID iDs

Joel N. Bregman ⦿ https://orcid.org/0000-0001-6276-9526
Michael E. Anderson ⦿ https://orcid.org/0000-0002-1661-5689
Matthew J. Miller ⦿ https://orcid.org/0000-0001-5448-7692
Edmund Hodges-Kluck ⦿ https://orcid.org/0000-0002-2397-206X
Xinyu Dai ⦿ https://orcid.org/0000-0001-9203-2808
Jiang-Tao Li ⦿ https://orcid.org/0000-0001-6239-3821
Yunyang Li ⦿ https://orcid.org/0000-0002-4820-1122
Zhijie Qu ⦿ https://orcid.org/0000-0002-2941-646X

References

Abitbol, M. H., Ahmed, Z., Barron, D., et al. 2017, arXiv:1706.02464
Anderson, M. E., & Bregman, J. N. 2010, ApJ, 714, 320
Anderson, M. E., & Bregman, J. N. 2011, ApJ, 737, 22
Anderson, M. E., & Bregman, J. N. 2014, ApJ, 785, 67
Anderson, M. E., Bregman, J. N., & Dai, X. 2013, ApJ, 762, 106
Anderson, M. E., Churazov, E., & Bregman, J. N. 2016, MNRAS, 455, 227
Anderson, M. E., Gaspari, M., White, S. D. M., Wang, W., & Dai, X. 2015, MNRAS, 449, 3806
Arnaud, M., Pratt, G. W., Piffaretti, R., et al. 2010, A&A, 517, A92
Athey, A. E. 2007, PhD thesis, Univ. of Michigan
Barber, C., Starkenburg, E., Navarro, J. F., McConnachie, A. W., & Fattahi, A. 2014, MNRAS, 437, 959
Barcons, X. 2015, Exploring the Hot and Energetic Universe: The First Scientific Conference Dedicated to the Athena X-ray Observatory, 10, http://www.cosmos.esa.int/web/conferences-archive/athena-2015
Behroozi, P. S., Conroy, C., & Wechsler, R. H. 2010, ApJ, 717, 379
Bernardi, M., Shankar, F., Hyde, J. B., et al. 2010, MNRAS, 404, 2087
Bland-Hawthorn, J., & Gerhard, O. 2016, ARA&A, 54, 529
Blanton, M. R., Schlegel, D. J., Strauss, M. A., et al. 2005, AJ, 129, 2562
Bogdán, Á., Forman, W. R., Vogelsberger, M., et al. 2013, ApJ, 772, 97
Bogdán, Á., Vogelsberger, M., Kraft, R. P., et al. 2015, ApJ, 804, 72
Borthakur, S., Heckman, T., Tumlinson, J., et al. 2015, ApJ, 813, 46
Borthakur, S., Heckman, T., Tumlinson, J., et al. 2016, ApJ, 833, 259
Bourne, N., Maddox, S. J., Dunne, L., et al. 2012, MNRAS, 421, 3027
Bovy, J., Nidever, D. L., Rix, H.-W., et al. 2014, ApJ, 790, 127
Bowen, D. V., Pettini, M., & Blades, J. C. 2002, ApJ, 580, 169
Bregman, J. N., Alves, G. C., Miller, M. J., & Hodges-Kluck, E. 2015, JATIS, 1, 045003
Busha, M. T., Evrard, A. E., Adams, F. C., & Wechsler, R. H. 2005, MNRAS, 363, L11
Carlstrom, J. E., Ade, P. A. R., Aird, K. A., et al. 2011, PASP, 123, 568
Cavaliere, A., & Fusco-Femiano, R. 1976, A&A, 49, 137
Crain, R. A., Schaye, J., Bower, R. G., et al. 2015, MNRAS, 450, 1937
Dai, X., Anderson, M. E., Bregman, J. N., & Miller, J. M. 2012, ApJ, 755, 107
Davé, R., Finlator, K., & Oppenheimer, B. D. 2011, MNRAS, 416, 1354
David, L. P., Jones, C., Forman, W., Vargas, I. M., & Nulsen, P. 2006, ApJ, 653, 207
Davis, D. S., & White, R. E., III 1996, ApJL, 470, L35
Emerick, A., Mac Low, M.-M., Grcevich, J., & Gatto, A. 2016, ApJ, 826, 148
Faerman, Y., Sternberg, A., & McKee, C. F. 2017, ApJ, 835, 52
Fang, T., Bullock, J., & Boylan-Kolchin, M. 2013, ApJ, 762, 20
Fang, T., Buote, D., Bullock, J., & Ma, R. 2015, ApJS, 217, 21
Feldmann, R., Hooper, D., & Gnedin, N. Y. 2013, ApJ, 763, 21
Fielding, D., Quataert, E., McCourt, M., & Thompson, T. A. 2017, MNRAS, 466, 3810
Ford, H. A., & Bregman, J. N. 2016, in IAU Symp. 315, From Interstellar Clouds to Star-forming Galaxies: Universal Processes? (Cambridge: Cambridge Univ. Press), E21
Fukugita, M., & Peebles, P. J. E. 2006, ApJ, 639, 590
Gaskin, J., Özel, F., & Vikhlinin, A. 2016, Proc. SPIE, 9904, 99040N
Gaspari, M., Brighenti, F., Temi, P., & Ettori, S. 2014, ApJL, 783, L10
Gnedin, O. Y., Brown, W. R., Geller, M. J., & Kenyon, S. J. 2010, ApJL, 720, L108
Goulding, A. D., Greene, J. E., Ma, C.-P., et al. 2016, ApJ, 826, 167
Gray, W. J., Scannapieco, E., & Kasen, D. 2015, ApJ, 801, 107
Greco, J. P., Hill, J. C., Spergel, D. N., & Battaglia, N. 2015, ApJ, 808, 151
Guo, Q., White, S., Li, C., & Boylan-Kolchin, M. 2010, MNRAS, 404, 1111
Gupta, A., Mathur, S., Galeazzi, M., & Krongold, Y. 2014, Ap&SS, 352, 775
Gupta, A., Mathur, S., Krongold, Y., Nicastro, F., & Galeazzi, M. 2012, ApJL, 756, L8
Haardt, F., & Madau, P. 2012, ApJ, 746, 125
Henley, D. B., & Shelton, R. L. 2012, ApJS, 202, 14
Henley, D. B., & Shelton, R. L. 2013, ApJ, 773, 92
Hernández-Monteagudo, C., Ma, Y.-z., Kitaura, F.-S., et al. 2015, PhRvL, 115, 191301
Hodges-Kluck, E. J., Miller, M. J., & Bregman, J. N. 2016, ApJ, 822, 21
Humphrey, P. J., Buote, D. A., Canizares, C. R., Fabian, A. C., & Miller, J. M. 2011, ApJ, 729, 53
Humphrey, P. J., Buote, D. A., Gastaldello, F., et al. 2006, ApJ, 646, 899
Humphrey, P. J., Buote, D. A., O'Sullivan, E., & Ponman, T. J. 2012, ApJ, 755, 166
Kauffmann, G., Borthakur, S., & Nelson, D. 2016, MNRAS, 462, 3751
Kaufmann, T., Bullock, J. S., Maller, A., & Fang, T. 2008, in ASP Conf. Ser. 396, Formation and Evolution of Galaxy Disks, ed. J. G. Funes, S. J., & E. M. Corsini (San Francisco, CA: ASP), 439
Keeney, B. A., Stocke, J. T., Danforth, C. W., et al. 2017, ApJS, 230, 6
Knapp, T. R. 2007, Journal of Modern Applied Statistical Methods, 6, 3
Le Brun, A. M. C., McCarthy, I. G., & Melin, J.-B. 2015, MNRAS, 451, 3868
Lehner, N., Howk, J. C., & Wakker, B. P. 2015, ApJ, 804, 79
Lehner, N., Howk, J. C., & Wakker, B. P. 2017, ApJ, 848, 71

Leitner, S. N., & Kravtsov, A. V. 2011, ApJ, 734, 48
Li, J.-T., Bregman, J. N., Wang, Q. D., Crain, R. A., & Anderson, M. E. 2016, ApJ, 830, 134
Li, J.-T., Bregman, J. N., Wang, Q. D., et al. 2017, ApJS, 233, 20
Li, J.-T., Bregman, J. N., Wang, Q. D., Crain, R. A., & Anderson, M. E. 2018, ApJL, 855, L24
Li, Y., & Bregman, J. 2017, ApJ, 849, 105
Loewenstein, M., & White, R. E., III 1999, ApJ, 518, 50
Ma, Y.-Z., Van Waerbeke, L., Hinshaw, G., et al. 2015, JCAP, 9, 046
McCammon, D., Almy, R., Apodaca, E., et al. 2002, ApJ, 576, 188
McGaugh, S. S., Schombert, J. M., de Blok, W. J. G., & Zagursky, M. J. 2010, ApJL, 708, L14
Miller, M. J., & Bregman, J. N. 2013, ApJ, 770, 118
Miller, M. J., & Bregman, J. N. 2015, ApJ, 800, 14
Miller, M. J., & Bregman, J. N. 2016, ApJ, 829, 9
Miller, M. J., Hodges-Kluck, E. J., & Bregman, J. N. 2016, ApJ, 818, 112
Morselli, L., Renzini, A., Popesso, P., & Erfanianfar, G. 2016, MNRAS, 462, 2355
Moster, B. P., Somerville, R. S., Maulbetsch, C., et al. 2010, ApJ, 710, 903
Navarro, J. F., Frenk, C. S., & White, S. D. M. 1997, ApJ, 490, 493
Nevalainen, J., Wakker, B., Kaastra, J., et al. 2017, A&A, 605, A47
Nicastro, F., Senatore, F., Krongold, Y., Mathur, S., & Elvis, M. 2016, ApJL, 828, L12
Nicastro, F., Zezas, A., Drake, J., et al. 2002, ApJ, 573, 157
O'Sullivan, E., & Ponman, T. J. 2004, MNRAS, 354, 935
O'Sullivan, E., Sanderson, A. J. R., & Ponman, T. J. 2007, MNRAS, 380, 1409
Pellegrini, S. 2011, ApJ, 738, 57
Piontek, F., & Steinmetz, M. 2011, MNRAS, 410, 2625
Pisano, D. J. 2014, AJ, 147, 48
Planck Collaboration, Ade, P. A. R., Aghanim, N., et al. 2013, A&A, 557, A52
Planck Collaboration, Ade, P. A. R., Aghanim, N., et al. 2014, A&A, 571, A16
Planck Collaboration, Ade, P. A. R., Aghanim, N., et al. 2016, A&A, 586, A140
Prochaska, J. X., Werk, J. K., Worseck, G., et al. 2017, ApJ, 837, 169
Putman, M. E. 2017, ASSL, 430, 1
Putman, M. E., Peek, J. E. G., & Joung, M. R. 2012, ARA&A, 50, 491
Qu, Z., & Bregman, J. N. 2018, ApJ, 856, 5

Rasmussen, A., Kahn, S. M., & Paerels, F. 2003, in ASSL Conf. Proc. 281, The IGM/Galaxy Connection. The Distribution of Baryons at z = 0, ed. J. L. Rosenberg & M. E. Putman (Dordrecht: Kluwer), 109
Reid, M. J., Menten, K. M., Brunthaler, A., et al. 2014, ApJ, 783, 130
Roberts, M. S., & Haynes, M. P. 1994, ARA&A, 32, 115
Salem, M., Besla, G., Bryan, G., et al. 2015, ApJ, 815, 77
Sancisi, R., Fraternali, F., Oosterloo, T., & van der Hulst, T. 2008, A&ARv, 15, 189
Scannapieco, C., Wadepuhl, M., Parry, O. H., et al. 2012, MNRAS, 423, 1726
Schaller, M., Frenk, C. S., Bower, R. G., et al. 2015, MNRAS, 451, 1247
Smith, R. K., Abraham, M. H., Allured, R., et al. 2016, Proc. SPIE, 9905, 99054M
Sokołowska, A., Mayer, L., Babul, A., Madau, P., & Shen, S. 2016, ApJ, 819, 21
Stocke, J. T., Keeney, B. A., Danforth, C. W., et al. 2013, ApJ, 763, 148
Stocke, J. T., Keeney, B. A., Danforth, C. W., et al. 2014, ApJ, 791, 128
Stocke, J. T., Keeney, B. A., Danforth, C. W., et al. 2017, ApJ, 838, 37
Swetz, D. S., Ade, P. A. R., Amiri, M., et al. 2011, ApJS, 194, 41
Taylor, J. E., Moodley, K., & Diego, J. M. 2003, MNRAS, 345, 1127
Tepper-García, T., Bland-Hawthorn, J., & Sutherland, R. S. 2015, ApJ, 813, 94
Tozzi, P., & Norman, C. 2001, ApJ, 546, 63
Van Waerbeke, L., Hinshaw, G., & Murray, N. 2014, PhRvD, 89, 023508
Velander, M., van Uitert, E., Hoekstra, H., et al. 2014, MNRAS, 437, 2111
Vikhlinin, A., Kravtsov, A., Forman, W., et al. 2006, ApJ, 640, 691
Vogelsberger, M., Genel, S., Springel, V., et al. 2014, MNRAS, 444, 1518
Walker, S. A., Bagchi, J., & Fabian, A. C. 2015, MNRAS, 449, 3527
Wang, Q. D., Yao, Y., Tripp, T. M., et al. 2005, ApJ, 635, 386
Wang, W., White, S. D. M., Mandelbaum, R., et al. 2016, MNRAS, 456, 2301
Watkins, L. L., Evans, N. W., & An, J. H. 2010, MNRAS, 406, 264
Werk, J. K., Prochaska, J. X., Thom, C., et al. 2013, ApJS, 204, 17
Werk, J. K., Prochaska, J. X., Tumlinson, J., et al. 2014, ApJ, 792, 8
White, S. D. M., & Frenk, C. S. 1991, ApJ, 379, 52
White, S. D. M., & Rees, M. J. 1978, MNRAS, 183, 341
Williams, R. J., Mathur, S., Nicastro, F., et al. 2005, ApJ, 631, 856
Wilman, D. J., & Erwin, P. 2012, ApJ, 746, 160
Xue, X. X., Rix, H. W., Zhao, G., et al. 2008, ApJ, 684, 1143
Yao, Y., Wang, Q. D., Hagihara, T., et al. 2009, ApJ, 690, 143
Zheng, Y., Putman, M. E., Peek, J. E. G., & Joung, M. R. 2015, ApJ, 807, 103